Thermoreflectance for the Instantaneous Measurement of Temperature at a Wall-Vapor Interface

by

Jason Chan

A thesis submitted in partial fulfillment of
the requirements for the degree of

Master of Science
(Mechanical Engineering)

at the

University of Wisconsin-Madison

2020

Thermoreflectance for the Instantaneous Measurement of Temperature at a Wall-Vapor Interface

Jason Chan, Master of Science
Department of Mechanical Engineering
University of Wisconsin-Madison, 2020
Professor Gregory F. Nellis, Advisor
Arganthaël Berson, Co-advisor
Kristofer Dressler, Co-advisor

Annular flow is a two-phase internal flow regime consisting of a vapor core with entrained droplets, surrounded by a thin liquid film. This type of flow is very common in heat exchanger systems. At high heat flux, the liquid film may dry out, resulting in a sharp reduction in the heat transfer coefficient of the flow. During the transition to complete dryout, cyclic re-wetting and dryout events are observed. Our long term goal is to characterize the heat transfer during these cyclic dryout events and to better understand what triggers the transition to dryout completion.

To characterize heat transfer during these cyclic dryout events, a non-invasive and instantaneous optical thermometry technique based on thermoreflectance was developed. This technique infers the temperature at the wall-vapor interface by measuring the reflectance of an incident laser beam—an optical quantity dependent on the vapor density and incident beam angle. By combining this technique with thermoreflectance at a wall-liquid interface and pressure measurements, the time-varying heat-transfer coefficient during cyclic dryout events was estimated. Due to the small change in refractive index (± 0.0015) in the temperature and pressure range of interest, a highly rigid and accurate experimental setup has been designed to reduce noise in the measurements. Potential sources of error between experimental heat transfer coefficient data and a literature model were identified.

The R245fa working fluid used in this work does not have well-documented optical properties. A refractometer was developed as part of this work to provide accurate refractive index values as a function of fluid density. The method measures the critical angle of an incident point source of light at the interface of a glass substrate and the fluid, at various fluid densities. The resulting data from a validation process of the refractometer using 2-propanol—a fluid with well-known optical properties—show the promise of this method. Several sources of error that may cause discrepancies with published data are discussed.

Acknowledgments

I would like to thank my advisor and committee chair, Professor Greg Nellis, for his insightful guidance, calming presence, and the genuine interest in science that had always inspired me and my colleagues to carry on the often frustrating research. I am also thankful for my co-advisor, Arganthaël Berson, who has been there since day one, when I asked him for opportunities to work in a lab. It was that day he opened the door to my unique and eventful college career, where skills were honed and interests discovered. Thanks to Arganthaël's brilliant mind, every time he steps foot in the lab, I know I can count on him for a productive session of critical thinking and novel ideas that keeps me wondering about better ways to improve our research. Last, but certainly not least, I'd like to thank my other co-advisor, Kris Dressler, for his incredible patience and down-to-earth essence. Dress is the only person I know that can reliably re-explain a complex concept while using uniquely amazing (and often hilarious) analogies every time to illustrate his point. Though, with his exceptional ability to teach, once is typically needed.

I know all three of my advisors have my back, and for that, I am truly grateful.

Thank you, Professor Dakotah Thompson, for serving on my thesis committee and offering invaluable insight.

I would like to acknowledge the Naval Nuclear Laboratory for their financial support. Thank you to Evan Hurlburt and Louise McCarroll for their guidance with the project and entrusting our lab to complete the project right.

Thank you to the undergraduate research assistants, Dan, Evan, Sydney and Ian, for their contribution these past few years. Thank you, Roman, for having the patience to re-train me on operating the loop over the semesters, and for showing me the importance of a pragmatic approach to solving problems, especially when time and resources are scarce.

This work was possible only because of everyone's combined efforts and contributions. Thank you.

Table of Contents

Abstract **i**

Acknowledgments **ii**

Table of Contents **iii**

List of Tables **v**

List of Figures **v**

Nomenclature **ix**

1 Introduction **1**
1.1 Two-Phase Flow . . . 1
1.2 Annular Flow Heat Transfer Coefficient . . . 3
1.3 Test Section . . . 3
1.4 Wall-fluid Temperature Measurement . . . 4
1.4.1 Previous Work . . . 5

2 Vapor Thermoreflectance **7**
2.1 Optical Theory . . . 7
2.1.1 Density-dependent fluid refractive index . . . 7
2.1.2 Reflectance Model . . . 10
2.2 Experimental Setup . . . 15
2.2.1 Optomechanical Setup . . . 18
2.2.2 Prism refractive index . . . 19
2.3 Calibration Process . . . 25
2.3.1 Single-Phase Calibration . . . 25
2.4 Heat transfer . . . 30

3 Refractometer **35**
3.1 Optical theory . . . 35
3.2 Experimental setup . . . 37
3.3 Calibration Results . . . 41
3.4 Future Work . . . 44

4 Conclusion **46**

5 Appendix **49**
5.1 LabVIEW Control Program Revision . . . 49
5.1.1 Revision Principle . . . 49
5.1.2 Configuration . . . 50
5.1.3 Validation and Initialization . . . 52

5.1.4 Measurement Loop 54
5.1.5 Clean-up and Reset 61

List of Tables

1 Refractive index of test section optical materials, for the vapor TR setup, in the order encountered by the HeNe input laser beam (632.8 nm) at normal conditions (20°C, 1 atm) for modeling purposes. 17
2 Nominal test section conditions 32

List of Figures

1 Liquid flow in a heated channel and the associated heat transfer coefficient at the wall. The single-phase liquid transitions from saturated liquid to saturated vapor with entrained liquid droplets. Heat transfer coefficient at the wall, h_{tp}, increases with decreasing liquid film thickness until dryout occurs (i.e. mist flow). Figure from Kim and Mudawar [8]. 2
2 Cross section CAD rendering of the test section. Fluid flows in the direction perpendicular to the page through the center channel (orange) that is made out of polyetherimide. The top and bottom of the test section are covered with FTO-coated float glass sheets and clamped with aluminum plates (gray). 4
3 Light traveling from a slow to a fast medium produces an evanescent field near the interface in the fast medium before re-entering the slow medium as the reflected beam. Figure from [18]. 8
4 Curve fit of saturated R245fa refractive indices published by Schmidt et al. [14] with respect to the saturated vapor temperature using the Lorentz-Lorenz equation. Isobars from 80 to 200 kPa, the operating range of the test section, at temperatures up to 100°C show the small change in vapor refractive index. 9
5 Change in vapor R245fa refractive index with temperature at a reference temperature of 33°C. The most change in refractive index, at approximately 9E-5, for a 10°C change, occurs at 200 kPa. 10
6 Idealized schematic of the thermoreflectance concept. Due to the dissimilar refractive indices of the liquid and vapor phases of the fluid, different TR beam paths are needed to measure the temperature of each respective fluid at the wall. 11
7 Reflectance at the glass-vapor (R245fa) interface versus incident angle for s- and p-polarized beams. The maximum incident angle is the critical angle corresponding to the lower vapor refractive index (n=1.0005). The solid and dashed lines nearly overlay each other at most incident angles due to the small (0.0015) change in refractive index. The Brewster's angle, that is between 27° and 29°, can be used to verify the incident beam polarization. 13
8 The maximum optical sensitivity occurs at the limiting critical angle in the p-polarization—the beam polarization that should be used for the TR method. 14

9 Reflectance versus R245fa vapor refractive index at four incident angles on and about the critical angle in 0.04° increments. 15
10 Illustration of the material interfaces on the beam path for the vapor TR setup. Not to scale. 16
11 CAD rendering of the vertical TR configuration. The vertical configuration facilitates fine incident angle adjustments while the dovetail rail provides superior rigidity. The red line indicates the path of the laser beam emitting from the HeNe laser source. 19
12 Refractive index vs. temperature of N-BK7, the prism material. A difference in prism refractive index of 0.014 between 20 and 100°C affects the vapor TR model. 20
13 Illustration of the change in laser beam path with prism temperature. 1. The fixed input beam is nominally set at a 29-degree incident angle. 2. Following the blue reference beam path, the beam first reflects at the glass-fluid interface, then reaches the pre-aligned photodetector at the output prism face. 3. As the prism heats up, the beam deviates from the reference path, potentially becoming misaligned with the photodetector. The reflectance at the glass-fluid interface also changes due to the changed path and glass refractive index. 4. Assuming the photodetector is wide enough to capture the deviated beam, an effective input beam angle can be calculated to adjust for the changed glass refractive index. 21
14 P-reflectance at the glass-vapor interface vs. prism temperature at three saturated vapor temperatures. An ideal TR setup would indicate constant reflectance values for saturated vapors at constant temperatures. Compared to their expected constant values, the three curves show as much as 80% error, which can be accounted for by $\theta_{\text{air,corrected}}$. 23
15 P-reflectance at the glass-vapor interface vs. isothermal saturated vapor and prism temperatures, plotted with and without adjustment for the changing glass/prism temperature. This figure demonstrates the worst case scenario of error in measuring vapor temperature. 24
16 The left plot shows a 2D map of the propagated uncertainty in superheated (1 to 40°C) R245fa vapor density as a function of pressure and temperature. At pressure transducer and thermocouple uncertainties of 1.7 kPa and 1 K, the maximum uncertainty of 0.11 kg/m^3 occurs at a higher pressure, near the vapor saturation line (top-left corner). The right plot shows the percent contribution of uncertainty from the thermocouple measurement. 26
17 Intensity ratio versus density of vapor R245fa. 27
18 The 95% confidence interval of the density by intensity ratio is ±0.015 kg/m^3. The narrow confidence interval near the ends is due to the large sample size in that region and the random noise distorting the normal distribution assumption. That is, the samples in bins near the two ends are not normally distributed. 27

19 The density data ($\bar{s}_\rho = 0.0586$ kg/m^3) was discretized by intensity ratio ($\bar{s}_{ir} = 7.831\text{e}-4$) into 100 bins that are sufficiently populated (>100) to assume nearly normal distributions for z- scores to be used appropriately. 28
20 An example of the vapor density-intensity ratio calibration curve. The external wall temperature corresponding to the curve fit ranges from 32 to 36°C. 29
21 Instantaneous heat transfer coefficient with liquid, vapor, and external wall temperatures overlaid. Both the liquid and vapor TR setups were used to collect this data. 30
22 The HTC and wall temperature of cyclic re-wetting events over a 4 second period at a nearly constant external window temperature shows the potential of the vapor TR setup. 31
23 The Dittus-Boelter heat transfer coefficients underestimate the transient values calculated from experimental data by a factor of five. Three theories for explaining this discrepancy are proposed. 34
24 Illustration of the optical setup for the refractometer. Not to scale. . . . 36
25 Reflectance at the FTO-vapor interface of s-polarized ($R_\perp$), evenly polarized (R), and p-polarized ($R_{//}$) beams. The steady increase in reflectance of a beam before the critical angle leads to a less defined light ring. . . . 37
26 Light ring caused by the critical angle. As light rays propagate to the FTO-vapor interface, some are reflected and some are transmitted. Incident rays that are close to and above the critical angle are reflected and create a light ring. 38
27 Refractometer setup. The laser beam passes through a hole in the mirror before reaching the diffusing white tape on the test cell. The reflected image on the window is captured by the camera using the mirror. 39
28 Turning mirror with an on-axis through hole. The through-hole allows the incident beam to pass through, while the mirror allows the reflected image to be captured by a camera. 39
29 Refractometer vapor cell. The cell temperature was controlled by a water-propylene-glycol mixture circulated through the copper coil from a temperature-controlled water bath. 40
30 Refractive index (n) of 2-propanol. The constant offset between the measured and published data suggests an error in the window thickness or refractive index. 41
31 Adjusted refractive index (n) of 2-propanol. 43
32 Effects of a finite incident beam diameter. Not to scale. 45
A5.1 List of sensors and their configurations. 50
A5.2 Block diagram of the Validation and Initialization section. Configurations are verified and variables are initialized here. 53
A5.3 Test section heater safety and control mechanisms 55
A5.4 Pulse generator heater and stepper motor safety and control mechanisms 56
A5.5 Facility at-a-glance 57

A5.6 Offset management front panel indicators 59
A5.7 Dedicated loop for Modbus communication with the PLC. 60
A5.8 Front panel controls of the liquid and vapor pumps. 60

Nomenclature

Symbol	Description
θ_c	critical angle
θ_i	input angle of incidence
θ_t	angle of transmittance
D	Diameter
G_g	Vapor mass flux
G_l	Liquid mass flux
I_{in}	light intensity from test section optics
I_{out}	light intensity into test section optics
k_g	Vapor thermal conductivity
k_l	Liquid thermal conductivity
n	real component of index of refraction
n_i	refractive index of first material
n_t	refractive index of second material
Pr_g	Vapor flow Prandtl number
Pr_l	Liquid flow Prandtl number
q''_{in}	heat flux at the wall
R_p, $R_{//}$	p-polarized Fresnel coefficient
R_s, $R_\perp$	s-polarized Fresnel coefficient
Re_g	Vapor flow Reynolds number
Re_l	Liquid flow Reynolds number
T_{sat}	saturation temperature

T_{wall}	wall temperature
EES	Engineering Equation Solver
FTO	Fluorine-doped Tin Oxide
HeNe	Helium-Neon laser
HTC	heat transfer coefficient
MFVAL	Multiphase Flow Visualization and Analysis Lab
N-BK7	Schott designation of Borosilicate Crown glass
POE	polyolester compressor oil
R	reflected light intensity

1 Introduction

Reliable and accurate temperature measurements with high spatial resolution are difficult to achieve. Thermocouples, thermistors, and resistance temperature detectors are readily available, but require direct contact between the probe and the measured object. Physical access is often not possible. When it is, direct contact can alter the thermal phenomena occurring on the object. To achieve accuracy with high spatial resolution, a non-contact method may be needed.

This work was motivated by the need to measure the instantaneous inner-wall temperature in a channel flow. Since direct contact thermometry methods would disrupt the flow, an alternative method was needed. The specific focus was the development of a non-contact optical method for measuring the temperature of vapor flow on a heated surface. Section 2 details the theory, experimental setup and calibration process of the method. At the end of the section, an application of the technique is described for inferring the heat transfer coefficient from the heated surface to the vapor.

The application involves measuring the vapor temperature of a substance with unknown optical properties. Specifically, the refractive index of the fluid as a function of density is not well documented in the literature. To address this need, the theory, experimental setup and preliminary results of a refractometer are discussed in Section 3.

1.1 Two-Phase Flow

Two-phase fluids surround us more often than we tend to realize. From the boiling pot of pasta water to the flowing refrigerant in air conditioner coils, to even the raindrops falling from the sky, physical phenomena where liquid and vapor co-exist are ubiquitous and often important aspects of life. Common as they are, two-phase phenomena are complex and not well understood. One such case is the heat transfer behavior of single-species two-phase flow.

Generally, in cooling applications involving two-phase flows, subcooled liquid is first introduced to a system. As the liquid flows through a heated pipe, it picks up thermal energy from the pipe walls and becomes saturated. Saturation defines a condition in which liquid and vapor phases co-exist at a constant pressure and temperature. With more heat transferred from the walls, the saturated fluid quality increases, and the flow can develop into several characteristic flow regimes, which are illustrated in Figure 1. The heat transfer coefficient (HTC) of the two-phase flow increases as long as a liquid film is present at the wall. The presence of the liquid film differentiates the annular flow regime and the dryout (or mist flow) regime. This annular flow regime before dryout, where the maximum HTC occurs, is of particular interest. Since the HTC defines the amount of heat transfer that is driven by a certain temperature difference between a solid surface and the surrounding fluid, for a fixed amount of heat flux (heat transfer per area), the higher the HTC, the smaller the temperature difference between the two medium. This type of high HTC is particularly important and desired for efficiently operating heat exchangers at a high heat flux.

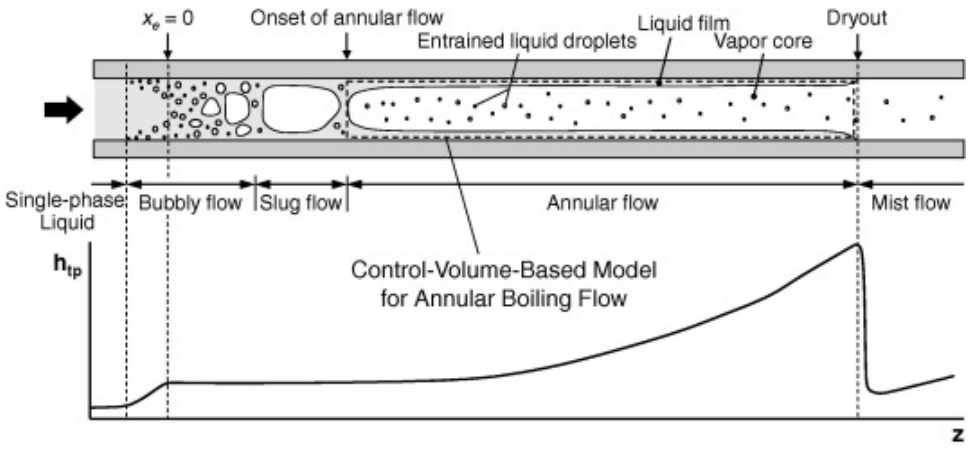

Figure 1: Liquid flow in a heated channel and the associated heat transfer coefficient at the wall. The single-phase liquid transitions from saturated liquid to saturated vapor with entrained liquid droplets. Heat transfer coefficient at the wall, h_{tp}, increases with decreasing liquid film thickness until dryout occurs (i.e. mist flow). Figure from Kim and Mudawar [8].

1.2 Annular Flow Heat Transfer Coefficient

Several events can occur after the liquid film dries out in an annular flow. On one hand, vapor flow at the wall could persist, and the less effective heat transfer associated with a vapor flow would result in an increasing wall temperature. This would be considered a sustained dryout. On the other hand, flow perturbations, such as an oscillating mass flux, could provide enough momentum for the liquid film to overcome the dryout point and rewet the pipe wall. This is referred to as cyclic-dryout.

A measure that characterizes the heat transfer during these events is critical to study the flow conditions that delineate the onset of each type of dryout. This measure is the HTC, which is defined by

$$HTC = \frac{q''}{T_{wall} - T_{\infty}} \tag{1}$$

where q'' is the wall heat flux, T_{∞} is the bulk fluid temperature, and T_{wall} is the wall temperature. In other words, the HTC is directly proportional to the heat flux for a given temperature difference. An accurate wall temperature measurement is critical for characterizing the HTC. However, it is difficult to perform this measurement without disturbing the liquid film with a typical thickness on the order of several hundred microns.

1.3 Test Section

The testing work in this study was carried out in the Annular Flow facility, which is part of the Multiphase Flow Visualization and Analysis Lab (MFVAL) at UW-Madison. The facility is capable of creating a two-phase flow by conditioning pentafluoropropane (also known as R245fa and HFC-245fa). The two-phase flow is contained within a 586 mm long rectangular duct with an inner cross section dimension of 12.00 x 36.25 mm. A CAD rendering of the test section cross section is shown in Figure 2. The center duct of the test section is made from a single piece of polyetherimide (PEI) duct (shown in

orange), and was designed to accept pressure transducers and fine-gauge thermocouples. The wide sides consist of two float glass windows (one for each side) that are clamped in place by aluminum plates and sealed with O-rings. A long slot was machined in each of the aluminum plates to allow optical access to the glass windows. The windows were manufactured by Delta Technologies and were coated with a thin fluorine-doped tin oxide (FTO) layer on the inner surface. The FTO coating is highly transparent in the visible spectrum and it is electrically conductive to function as a heater.

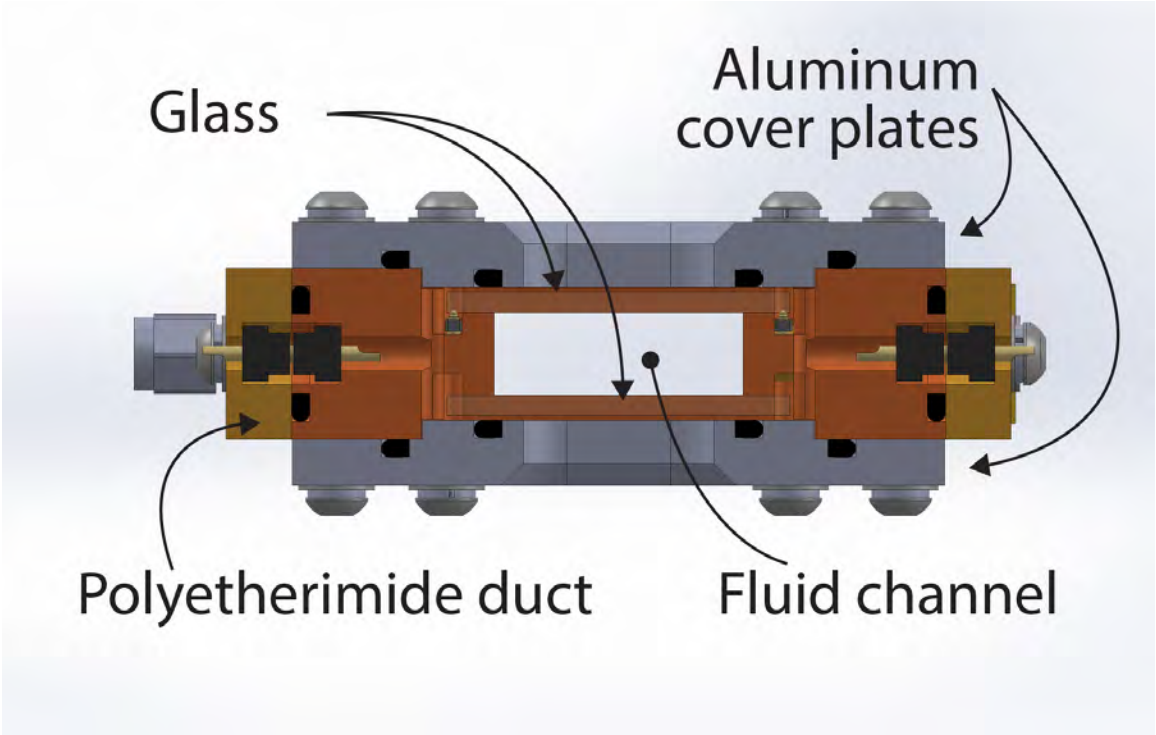

Figure 2: Cross section CAD rendering of the test section. Fluid flows in the direction perpendicular to the page through the center channel (orange) that is made out of polyetherimide. The top and bottom of the test section are covered with FTO-coated float glass sheets and clamped with aluminum plates (gray).

1.4 Wall-fluid Temperature Measurement

In order to characterize the heat transfer, we need to measure the inner wall temperature. A simple approach might be to use a thermocouple due to its relatively low cost and ease

of use. Yet, its need to make physical contact with the heated wall limits its use for this application. Similar arguments can be made against thermistors, hot-wire anemometers and any method that involves placing physical objects in the flow. Instead, a non-intrusive technique is needed. In this regard, infrared thermometry can be used [2, 12, 7]. However, without physical access to the target surface, the glass test section window needs to be infrared-transparent to achieve a high accuracy and a high time resolution. This is due to the absorption of infrared waves by opaque and semi-transparent substrates. When this type of substrate is used, the infrared radiation emitted at the target surface is partially absorbed and contaminated with the infrared emission by the substrate itself. A decontamination algorithm [2] would be needed to solve this problem. Without the algorithm, even with an infrared-transparent window, the method also requires a high-speed infrared camera that can be prohibitively expensive.

Alternatively, the thermoreflectance (TR) technique can be used. Instead of measuring infrared light, which can be readily absorbed and emitted by many surfaces, the TR technique is often used to measure the reflectance of light on a thin metal film at a specifically chosen optical wavelength. The sensitivity of this method is mostly determined by the thermoreflectance coefficient of the metal film. The typical TR implementation cannot be used on the test section, however, due to the conductive FTO coating which prevents the deposition of a thin metal film. Instead, the temperature-dependent refractive index of the fluid is measured directly.

1.4.1 Previous Work

Early development of the TR approach was done in the MFVAL by Shedd and Anderson [18]. They described a TR measurement technique that measures the diameter of a light ring reflected from the total internal reflection of a diffused light at the inner wall. Since the ring diameter is a function of the temperature-dependent liquid refractive index, the

wall-liquid temperature can be inferred by measuring the light ring diameter. While this method can be calibrated to produce measurements with uncertainties of less than ± 0.1 K, its application is limited by the single-phase requirement within the diameter of the light ring. In cases of a partial dryout, where liquid and vapor phases coexist at close proximity, the light ring would be segmented or completely obstructed.

Additional development of TR in the MFVAL was carried out by Rodarte [13, Section 8.2]. Instead of measuring light ring images, the intensity of the reflected beam was measured and compared to the incident beam intensity. The inner wall temperature can be inferred from the ratio of the two intensity measurements, i.e., the intensity ratio.

2 Vapor Thermoreflectance

The vapor thermoreflectance (TR) technique developed in this study is based on its liquid counterpart described by Fehring et al. [4]. In the original work, a laser beam is used to measure the temperature-dependent light reflectance at the wall-liquid interface, resulting in a non-invasive thermometry technique with a resolution on the order of 0.1 K.

2.1 Optical Theory

The development of the vapor TR technique makes use of optical theory and relies on a theoretical model to support calibration. The TR technique measures the density-dependent nature of fluid refractive indices, similar to a refractometer. Figure 3 illustrates the propagation of light waves at an optical interface where the temperature is to be measured. Shedd and Anderson [18] explain that when the incident beam is within approximately 10° of the critical angle, evanescent waves travel a short distance parallel to the interface in the lower refractive index material. The distance that evanescent waves propagate is generally on the order of a few wavelengths of the incident ray. Since these waves do not propagate as electromagnetic waves, but as spatially concentrated energy that exponentially decay in intensity with distance, their effective penetration depth into the fluid is on the order of 10 to 100 nm, according to solutions of Maxwell's equations in free space [11, 18]. While the evanescent wave theory is not explicitly included in the TR optical model, its penetration depth suggests the spatial resolution of the TR measurements.

2.1.1 Density-dependent fluid refractive index

The refractive index of a fluid is strongly dependent on its density [1]. For incompressible liquids with well established coefficients of thermal expansion, a relationship between its

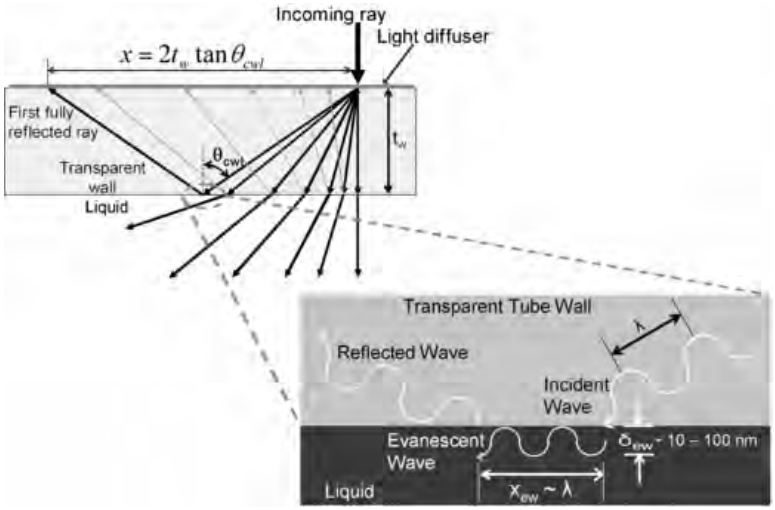

Figure 3: Light traveling from a slow to a fast medium produces an evanescent field near the interface in the fast medium before re-entering the slow medium as the reflected beam. Figure from [18].

temperature and refractive index can be readily developed. This was the case as described in Fehring et al. [4]. However, since vapor density is dependent on both pressure and temperature, its refractive index cannot be accurately modeled as only a function of temperature. The Lorentz–Lorenz equation

$$\begin{aligned} n &\approx \sqrt{1 + \frac{3AP}{RT}} \\ &= \sqrt{1 + \frac{3A\rho}{M}}, \text{ assuming Ideal Gas Law} \end{aligned} \tag{2}$$

relates the refractive index of a substance to its polarizability. For conditions where the Ideal Gas Law is valid, it relates the refractive index, n, to the molar refractivity, A, molecular weight, M, pressure, P, the universal gas constant, R, and absolute temperature, T. This equation can be rewritten in terms of the gas density, ρ, where the molar refractivity is the only unknown variable.

The molar refractivity is a measure of the total polarizability of a mole of a substance. Since the molar refractivity of the working fluid, R245fa, was not available in literature, it was used as a curve fitting parameter. Using the published refractive indices of saturated

R245fa vapor from Schmidt et al. [14], a curve-fit estimate of the refractive index at various temperatures and pressures is determined and shown in Figure 4. The estimated molar refractivity is 1.719E-5 m^3/mol.

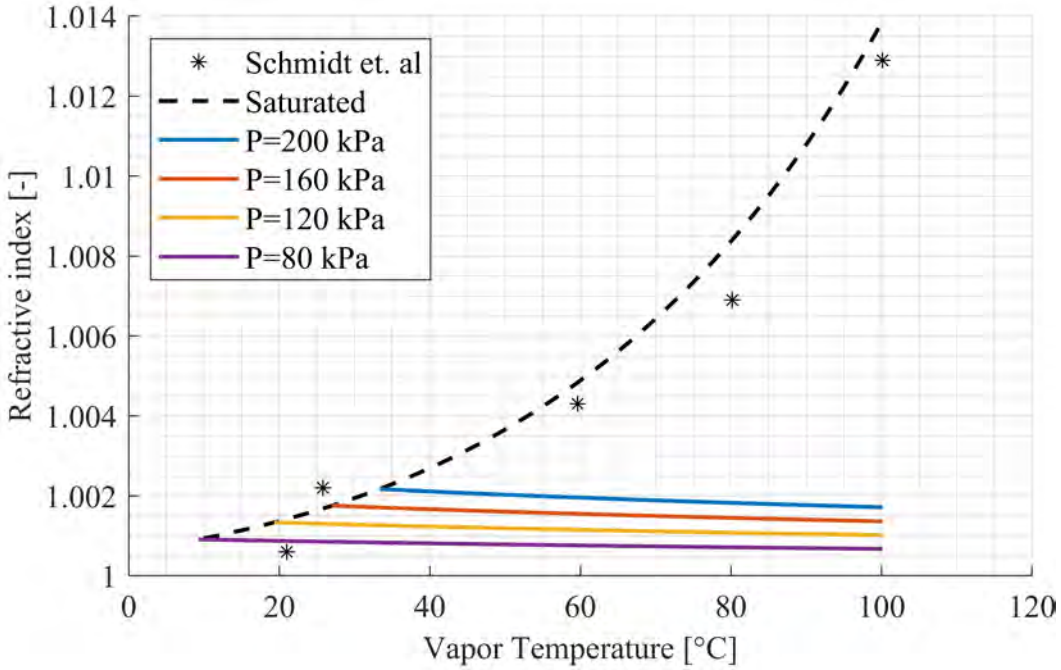

Figure 4: Curve fit of saturated R245fa refractive indices published by Schmidt et al. [14] with respect to the saturated vapor temperature using the Lorentz-Lorenz equation. Isobars from 80 to 200 kPa, the operating range of the test section, at temperatures up to 100°C show the small change in vapor refractive index.

The isobars in Figure 4 show a representative range of the operating pressure in the test section. At these pressures, the vapor refractive index is expected to vary by no more than 0.002 approximately between 1.0005 and 1.0020, across a temperature range from 20 to 100°C. Using 33°C as the reference temperature, the change in refractive index, Δn, with temperature, ΔT, is shown in Figure 5. The magnitude of the slope, $\frac{\Delta n}{\Delta T}$, is the sensitivity of refractive index to temperature, and it increases with pressure. At P=80 kPa, a change in 10°C results in an approximately 2E-5 change in refractive index, whereas at 200 kPa, the same change in temperature results in an approximately 9E-5 change in refractive index—a nearly 4 times increase.

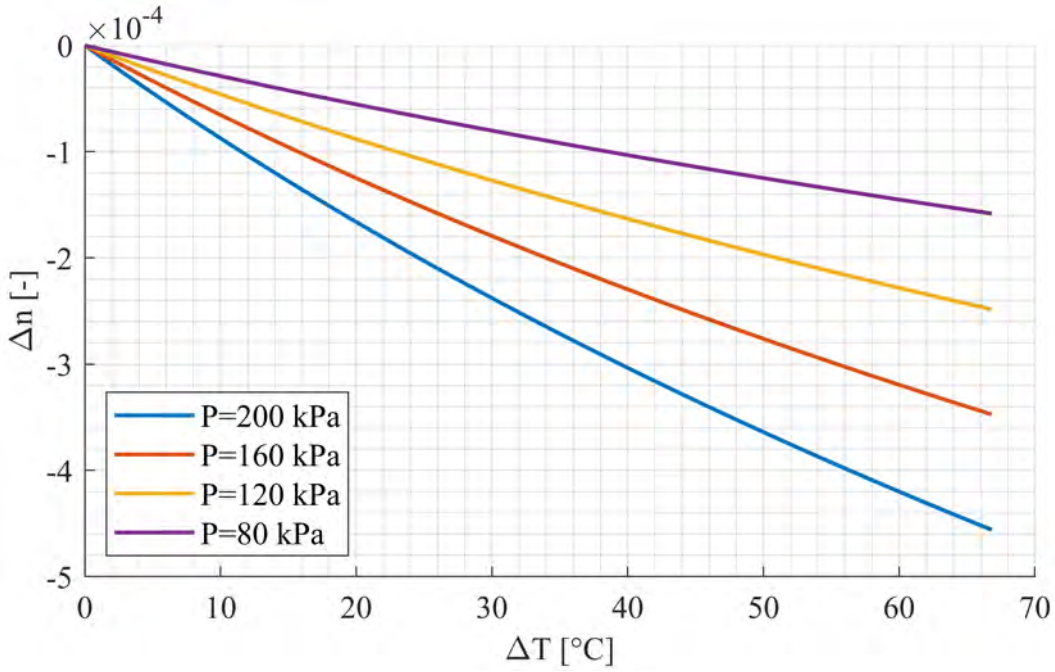

Figure 5: Change in vapor R245fa refractive index with temperature at a reference temperature of 33°C. The most change in refractive index, at approximately 9E-5, for a 10°C change, occurs at 200 kPa.

2.1.2 Reflectance Model

A simplified vapor TR model was constructed using the expected vapor refractive index. A schematic of the TR concept is shown in Figure 6. First, a light beam propagates through the prism and glass. The beam is then reflected at the fluid-glass interface, where the fluid refractive index is measured. Due to the dissimilar refractive indices of the liquid and vapor phases of the fluid, different TR beam paths are needed to measure the temperature of each respective fluid at the wall. A dedicated vapor TR setup is necessary to maximize the sensitivity of the optical measurement to vapor temperature changes. The reflectance measurement is governed by the Fresnel equations and Snell's law. The Fresnel equations

$$R_s = \left[\frac{n_1 cos(\theta_i) - n_2 cos(\theta_t)}{n_1 cos(\theta_i) + n_2 cos(\theta_t)}\right]^2 \tag{3a}$$

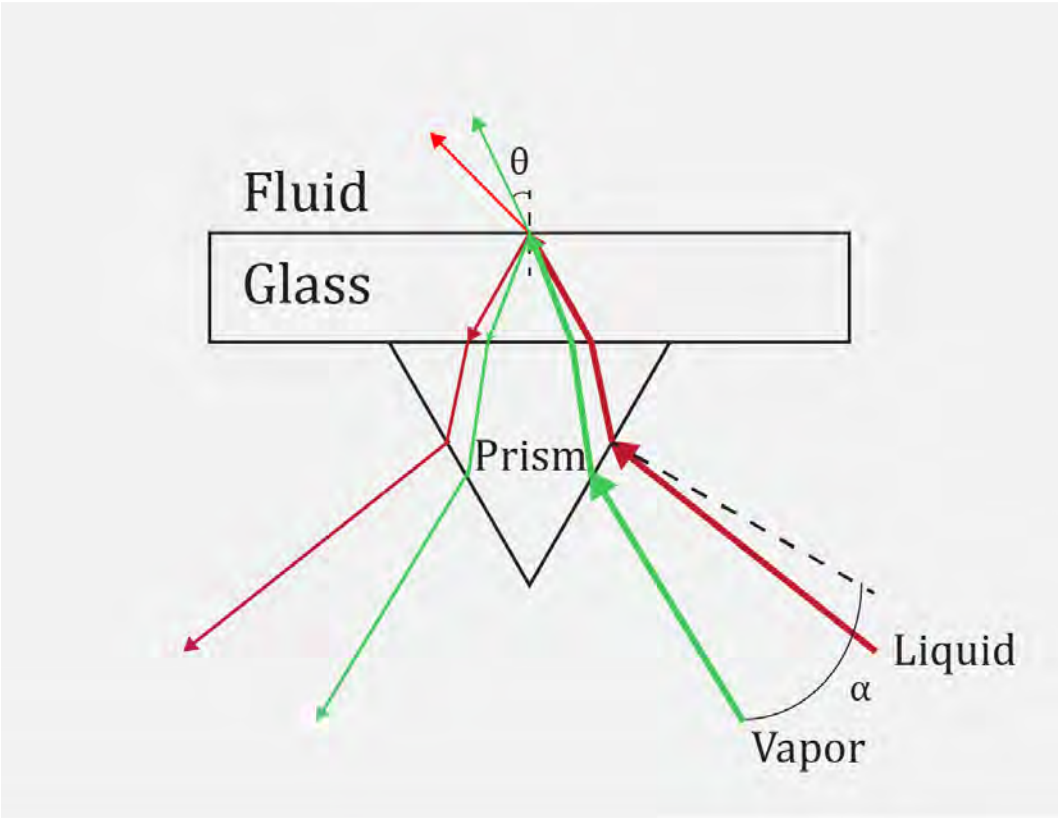

Figure 6: Idealized schematic of the thermoreflectance concept. Due to the dissimilar refractive indices of the liquid and vapor phases of the fluid, different TR beam paths are needed to measure the temperature of each respective fluid at the wall.

$$R_p = \left[\frac{n_2 cos(\theta_i) - n_1 cos(\theta_t)}{n_2 cos(\theta_i) + n_1 cos(\theta_t)}\right]^2 \tag{3b}$$

describe the reflected light intensity at an interface of different optical media as a function of the medium refractive indices, the incident angle, and the transmitted angle. The reflectance is also dependent on the wave polarization. Equation (3a) is the s-polarized reflectance and equation (3b) is the p-polarized reflectance. The polarization is commonly defined by the field direction with respect to the incident plane. A p-polarized beam has its field parallel to the incident plane, while a s-polarized beam is perpendicular to the incident plane. Both reflectance values are maximized at the critical angle, where

reflection occurs in totality. Snell's law

$$n_1 \cdot sin(\theta_i) = n_2 \cdot sin(\theta_t) \tag{4}$$

describes the relationship between incident and transmitted light angles. By setting θ_t to 90°, the critical angle for total internal reflection can be calculated ($\theta_i = \theta_{crit}$). These two equations are used simultaneously at every interface the laser beam passes through.

The TR sensitivity to changes in fluid density is related to the incident angle at the glass-vapor interface. The reflectance, as described by Equation 3, needs to be calculated with respect to the local incident beam angle. Since the inner surface of the test section window is coated with a conductive FTO layer, a refractive index of the FTO, $n = 1.85$, is used to model the glass. This value is used to calculate the reflectance at the glass-vapor interface with respect to the incident beam angle, as shown in Figure 7. Reflectance values for the minimum (n=1.0005, the solid line corresponds to high vapor temperature) and maximum (n=1.0020, the dashed line corresponds to low vapor temperature) vapor refractive indices are plotted for each beam polarization. Since the lower and upper bounds of operation are plotted, the expected reflectance range for a given incident angle can be determined. This is referred to as the optical sensitivity; the larger the reflectance change resulting from going from $n = 1.0005$ to $n = 1.0020$, the more sensitive the particular optical setup is.

For the vapor TR, due to the relatively small change in refractive index over the temperature (or density) range of interest, the sensitivity is less than 0.15 for incident angles below 32.7°. The sensitivity is maximized only when the incident angle approaches the critical angle corresponding to the expected lower limit of vapor refractive index ($n = 1.0005$). This is referred to as the limiting critical angle. Incident angles beyond the critical angle result in a decreased sensitivity for the given vapor refractive index range. Further, Figure 8 shows that a p-polarized beam is always preferred for the TR

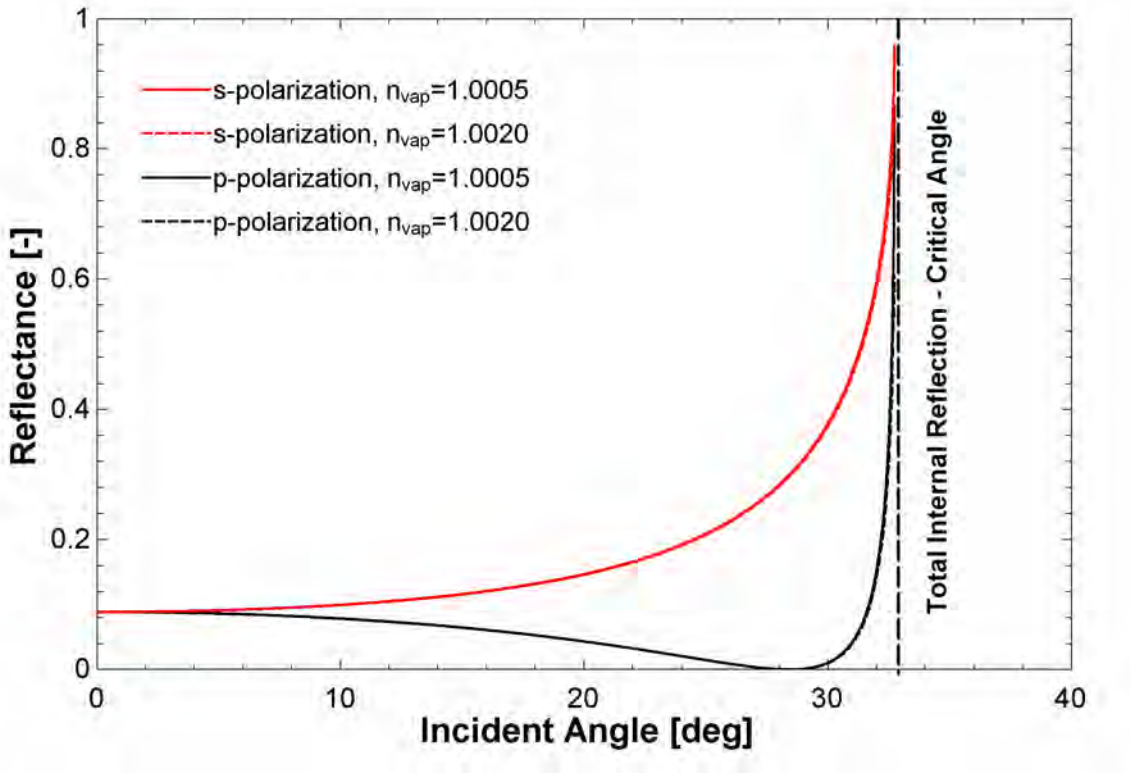

Figure 7: Reflectance at the glass-vapor (R245fa) interface versus incident angle for s- and p-polarized beams. The maximum incident angle is the critical angle corresponding to the lower vapor refractive index (n=1.0005). The solid and dashed lines nearly overlay each other at most incident angles due to the small (0.0015) change in refractive index. The Brewster's angle, that is between 27° and 29°, can be used to verify the incident beam polarization.

method to maximize sensitivity. As the incident angle approaches the critical angle from the left, the sensitivity corresponding to a p-polarized beam is greater than that of an s-polarized beam. The polarization direction of the incident beam can be verified by setting the incident beam to the Brewster's angle (between 27° and 29° in this case), at which point little to no reflection should be observed when the beam is p-polarized. The Brewster's angle, θ_B, is an incidence angle in which light with a particular polarization is perfectly transmitted to another dielectric medium, and is expressed by

$$\theta_B = \arctan(\frac{n_2}{n_1}) \tag{5}$$

where n_1 and n_2 are the refractive indices of the incident and transmitted media, respectively. The Fresnel equations predict this polarization to be parallel to the incidence plane.

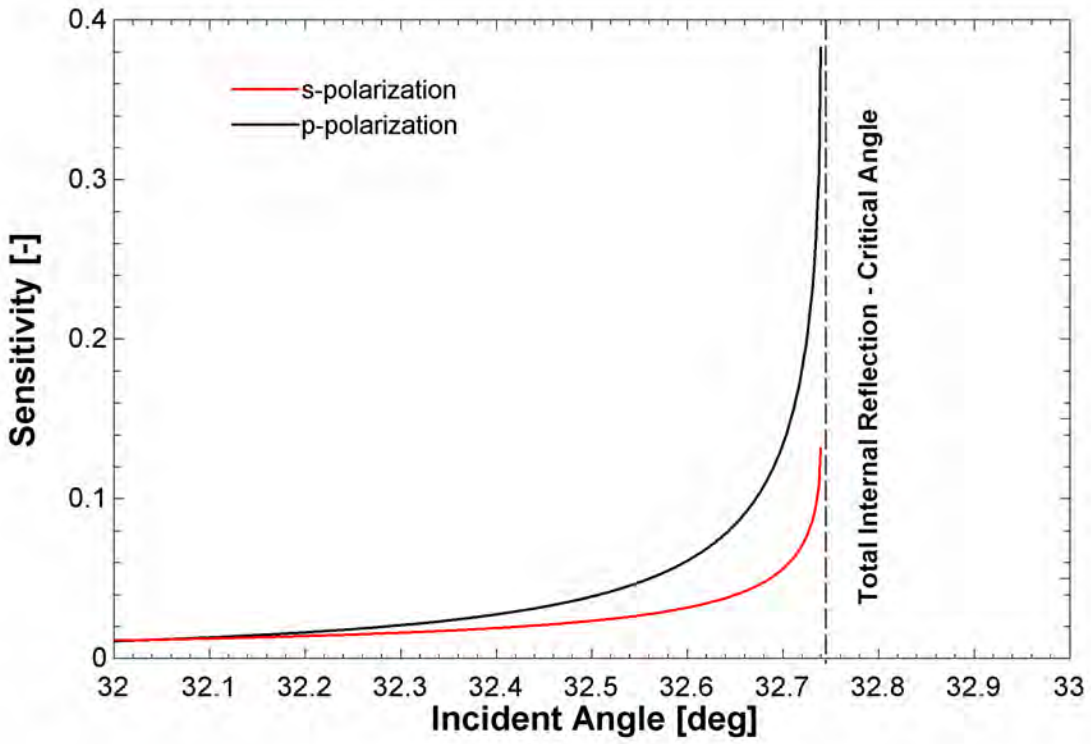

Figure 8: The maximum optical sensitivity occurs at the limiting critical angle in the p-polarization—the beam polarization that should be used for the TR method.

The results of a TR model for the aforementioned vapor refractive index range is shown in Figure 9. The model assumes a perfectly p-polarized beam at several incident angles, θ_i, about the critical angle. Due to the proximity of the vapor refractive index to unity, even in 0.04° increments, the reflectance can vary greatly; precision adjustments are needed in the experimental setup.

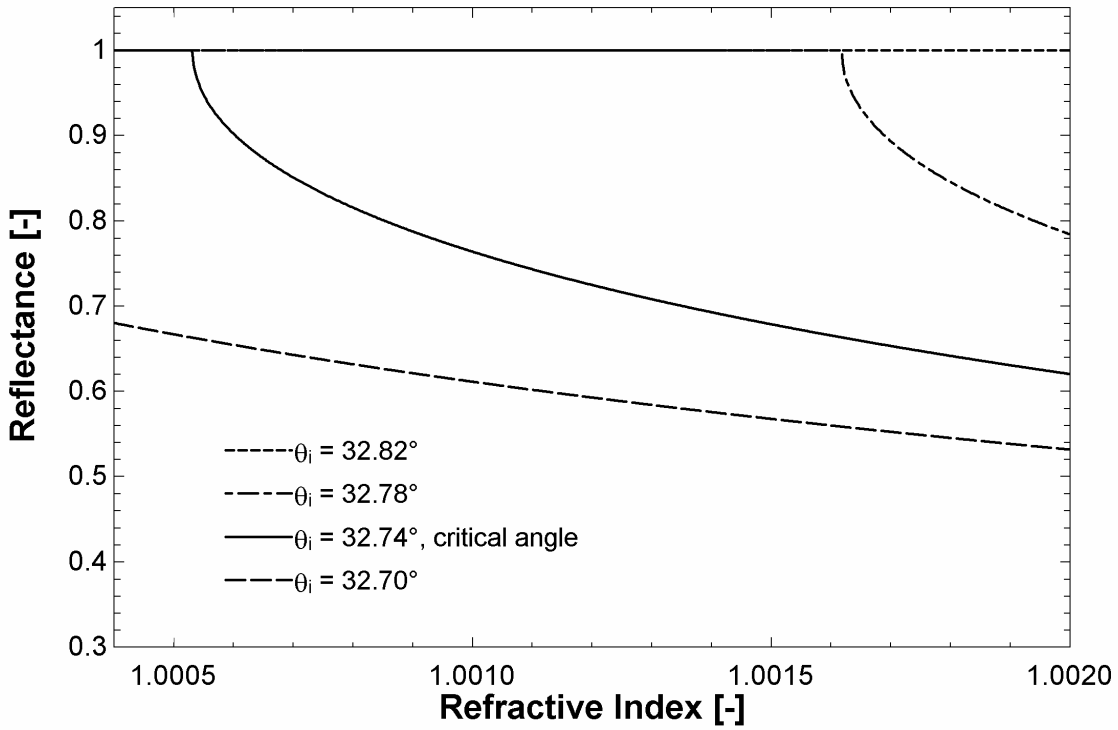

Figure 9: Reflectance versus R245fa vapor refractive index at four incident angles on and about the critical angle in 0.04° increments.

2.2 Experimental Setup

The vapor TR setup was constructed on the Annular Flow facility so measurements of the inner wall temperature of the fluid channel in the test section can be carried out. The experimental setup was modified from the optical model in Figure 6 to account for additional optical components in the laser path. First, an equilateral prism couples the free-space incident beam to the test section window. This is needed since a 32.74° incident beam at FTO-vapor interface cannot be achieved by simply directing a beam at a parallel glass (n=1.515) interface from air This was verfied according to Equation 4. Significant intensity losses would occur due to external reflection. The ideal and modified optical setups are illustrated in Figures 6 and 10, respectively. In the modified setup, the

prism is coupled to the glass window by an immersion fluid[1] with a matched refractive index. Further complicating the optical setup is the FTO coating on the inner walls of the test section windows. The electrically conductive FTO coating that is used as a heating element has a refractive index of approximately 1.85 at 633 nm, according to the glass window manufacturer, Delta Technologies. A thin layer of polyolester (POE) oil may also be present on top of the FTO coating. The POE oil is a lubricant commonly found in many refrigerants, including the R245fa manufactured by Honeywell. This combination of materials and optical interfaces are summarized in Figure 10, and their respective refractive indices are listed in Table 1.

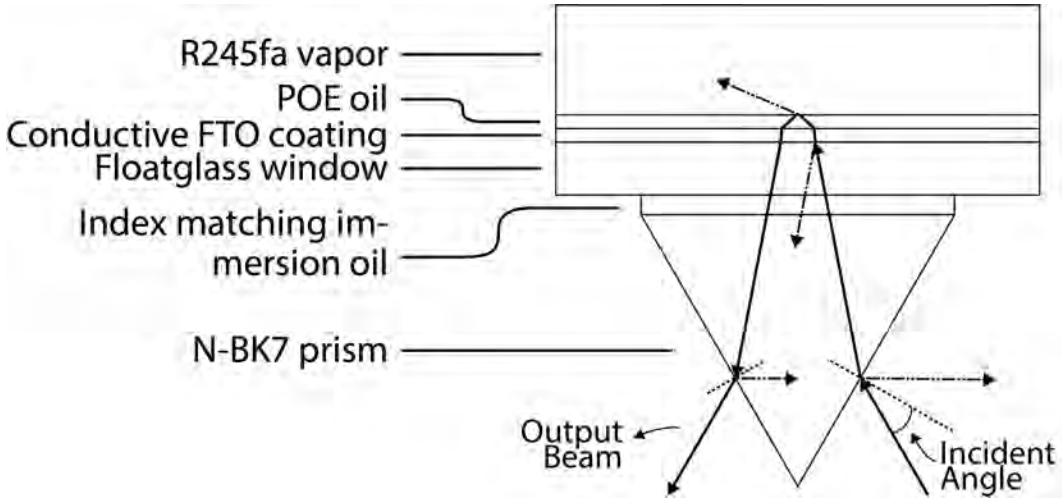

Figure 10: Illustration of the material interfaces on the beam path for the vapor TR setup. Not to scale.

The incident beam is emitted from a 10 mW HeNe laser source and directed at a prism face at a prescribed incident angle, θ_i. The beam then propagates through each material listed in Table 1. Similar to the aforementioned glass-vapor reflectance, the laser beam is reflected and refracted at every material interface along the optical path, where the expected reflectance at each interface can be determined by Equation 3. The reflectance at each interface is specified by two subscripts matching the corresponding

[1]Fisher Scientific Richard-Allan Scientific Resolve Immersion Oil, catalog #23-244267

Table 1: Refractive index of test section optical materials, for the vapor TR setup, in the order encountered by the HeNe input laser beam (632.8 nm) at normal conditions (20°C, 1 atm) for modeling purposes.

Order	Material	Refractive Index
1	Air	1.0002 [a]
2	N-BK7 Prism	1.515 [b]
3	Immersion Oil	1.515 [c]
4	Float Glass Window	1.52 [d]
5	FTO Coating	1.85 [d]
6	Polyolester Oil	1.4565 [e]
7	R245fa Vapor	1.010 [f]

[a] Ciddor [3]
[b] SCHOTT Advanced Optics [16]
[c] Fisher Scientific, catalog #23-244267
[d] Delta Technologies
[e] Semenyuk et al. [17]
[f] Nominal value using curve fit of data from Schmidt et al. [14]

value for each material in the first column of Table 1. The transmission at each interface is labeled similarly. For example, the reflectance at the air-prism interface is denoted as $R_{1,2}$, and the transmission $T_{1,2}$. Since the extinction coefficient of each material at 633 nm is negligibly small the reflectance and transmission at an interface between materials a and b sum up to unity, as described in Equation 6.

$$T_{a,b} + R_{a,b} = 1 \tag{6}$$

The composite ratio of input and output beam intensities is referred to as the intensity ratio, which can be formulated by propagating Equation 3 through the beam path. The incident and reflected beam intensities, I_{in} and $I_{reflected}$ respectively, in the forward direction from the air to the R245fa vapor layer are shown in Equation 7.

$$I_{reflected} = I_{in}(1 - R_{1,2})(1 - R_{2,3})(1 - R_{3,4})(1 - R_{4,5})(1 - R_{5,6})R_{6,7} \tag{7}$$

The reflected beam intensity at the oil-vapor interface, $I_{reflected}$, is propagated with sim-

ilar interface reflectance as the forward beam. The final output beam intensity, I_{out} is shown in Equation 8.

$$I_{out} = I_{reflected}(1 - R_{5,6})(1 - R_{4,5})(1 - R_{3,4})(1 - R_{2,3})(1 - R_{1,2}) \tag{8}$$

Combining Equations 7 and 8 yields the overall intensity ratio, IR as shown in Equation 9.

$$IR = \frac{I_{out}}{I_{in}} = [(1 - R_{1,2})(1 - R_{2,3})(1 - R_{3,4})(1 - R_{4,5})(1 - R_{5,6})]^2 R_{6,7} \tag{9}$$

2.2.1 Optomechanical Setup

The optomechanical rigidity of the vapor TR setup is critical to its capability to accurately measure the vapor density. As shown in Figure 9, for a given vapor refractive index, the expected reflectance at the glass-vapor interface can vary significantly due to changes in the incident beam angle that are as small as 0.04°. A vertical design was used in conjunction with a rigid dovetail rail system (Thorlabs #XT66-750) and micrometer-controlled manual rotation stage (Thorlabs #PR01) to allow direct control of adjusting the incident angle. The rotational stage has a fine adjustment resolution of 0.04°. Since the micrometer uses a vernier scale, at this vernier resolution, according to Thorlabs, an uncertainty of 20%, or 0.008°, can be appropriately assumed. A CAD rendering of the setup is shown in Figure 11. From the top left, a linearly polarized laser beam at 632.8 nm is introduced (shown in red) and directed at a silver-coated plano turning mirror. The beam then enters a polarizing beamsplitter cube (Thorlabs #CCM1-PBS252), where the s-polarized beam is reflected into a silicon switchable gain detector (Thorlabs # PDA36A2) while the p-polarized beam is transmitted to the prism.

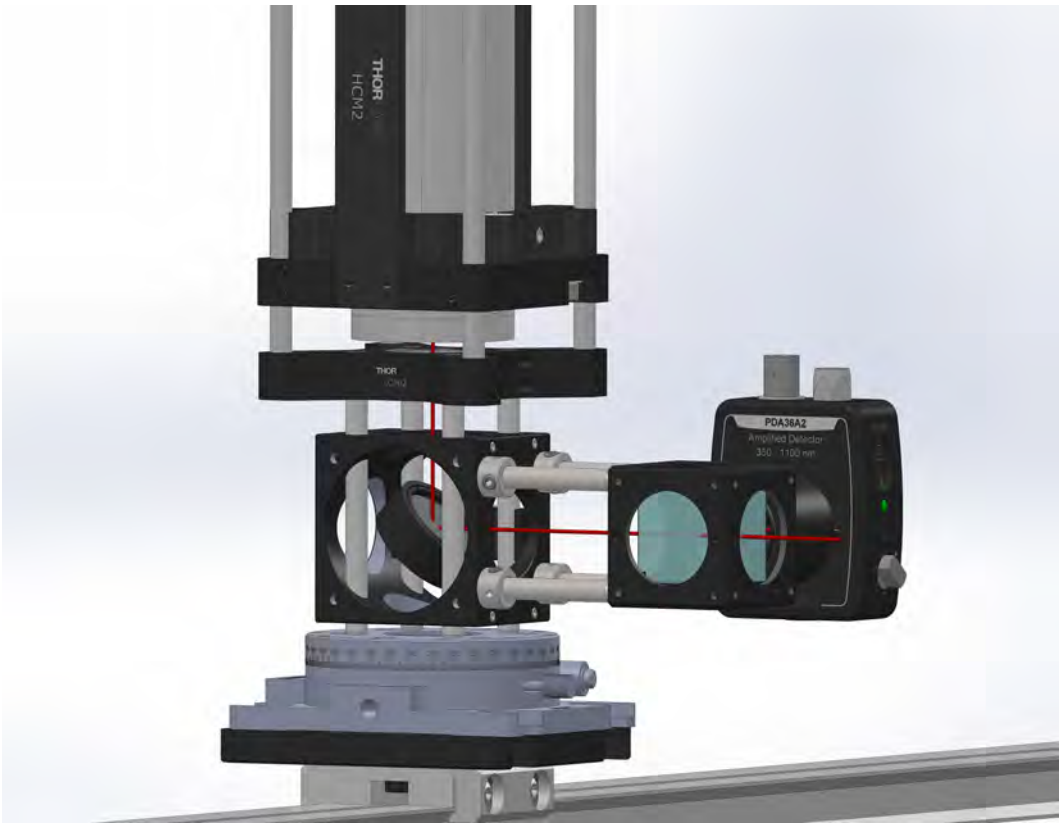

Figure 11: CAD rendering of the vertical TR configuration. The vertical configuration facilitates fine incident angle adjustments while the dovetail rail provides superior rigidity. The red line indicates the path of the laser beam emitting from the HeNe laser source.

2.2.2 Prism refractive index

The effects of a temperature-dependent prism refractive index cannot be neglected in the vapor TR measurements. Following the process published by Schott glass, the relationship between temperature and refractive index for N-BK7 is shown in Figure 12 [15, 16]. The 0.014 change in glass refractive index between 20 and 100°C is insignificant for the liquid TR measurements, but is important for the vapor measurements. The effect of the prism heating is further diminished as the liquid was rarely heated past approximately 40°C in experiments described in Fehring et al. [4].

This is not the case in the vapor TR setup. The weak temperature dependence of vapor refractive index amplifies the effect of changes in the incidence angle. In the vapor

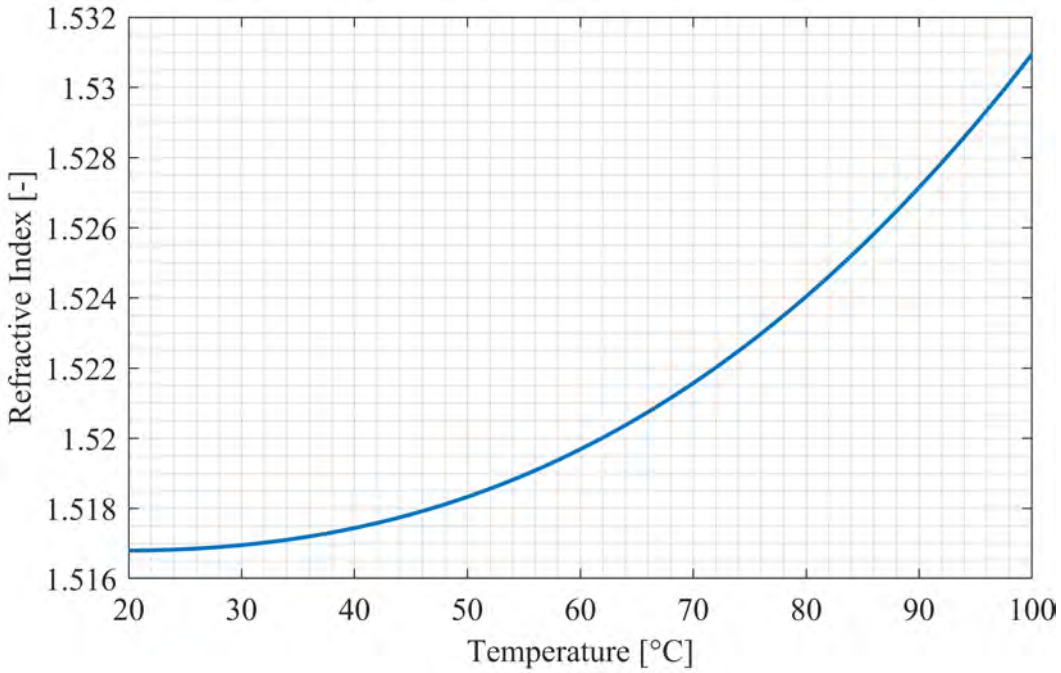

Figure 12: Refractive index vs. temperature of N-BK7, the prism material. A difference in prism refractive index of 0.014 between 20 and 100°C affects the vapor TR model.

setup, any change in the laser beam's incidence angle at the glass-vapor interface effectively distorts the calibration and can misalign the beam from the output photodetector. As a result, while the incident beam at the air-prism interface is stationary, the beam path changes in the prism with the changing prism temperature, as illustrated in Figure 13. The prism temperature changes due to the heated inner wall of the test section.

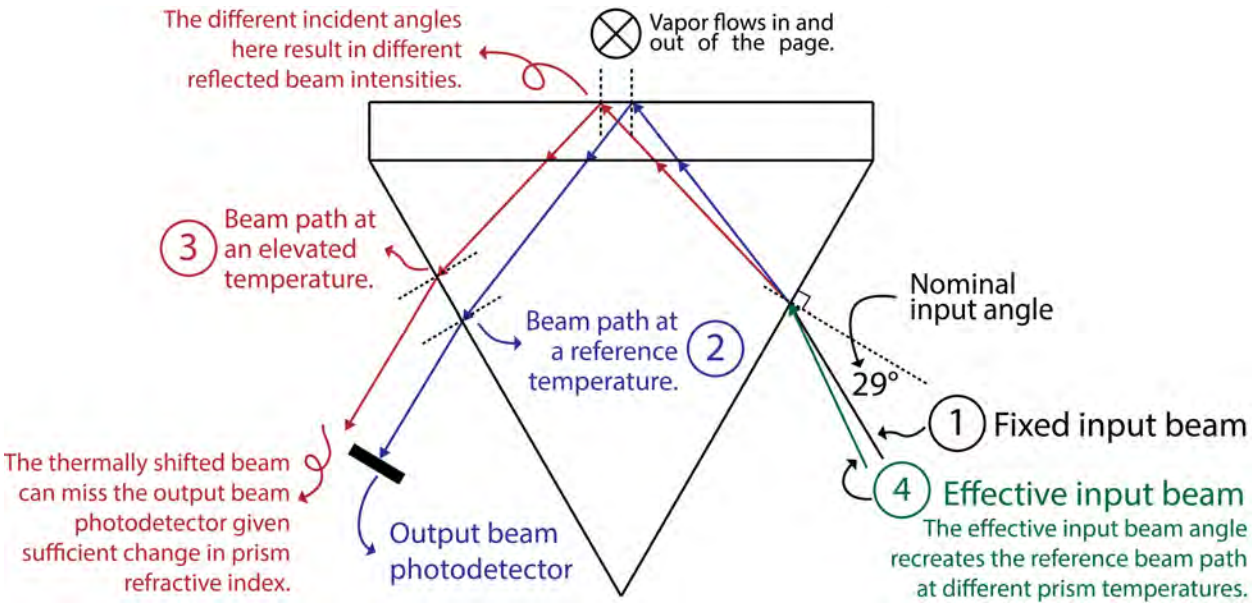

Figure 13: Illustration of the change in laser beam path with prism temperature. 1. The fixed input beam is nominally set at a 29-degree incident angle. 2. Following the blue reference beam path, the beam first reflects at the glass-fluid interface, then reaches the pre-aligned photodetector at the output prism face. 3. As the prism heats up, the beam deviates from the reference path, potentially becoming misaligned with the photodetector. The reflectance at the glass-fluid interface also changes due to the changed path and glass refractive index. 4. Assuming the photodetector is wide enough to capture the deviated beam, an effective input beam angle can be calculated to adjust for the changed glass refractive index.

One way to account for the changing glass refractive index is to use a corrected version of an independent variable. In this case, the corrected variable is the incident angle at the air-prism interface, $\theta_{\text{air,adjusted}}$. This corrected incident angle adjusts the measured reflectance at the wall-fluid interface to the correct value, as if the prism stayed at the reference temperature.

Equation (10a) relates the refractive indices (n) of air, glass and vapor refrigerant, and the incident angles (θ) at the relevant interfaces by assuming a constant prism refractive index. The corrected incident beam angle, $\theta_{\text{air,corrected}}$, can be calculated by maintaining the beam path through the glass-vapor interface. This is shown in Equation (10b), where n'_{vapor} denotes the temperature-adjusted prism refractive index. The glass-temperature-dependent p-polarization reflectance is compared to its corrected constant values from 20 to 70°C at three saturated vapor conditions, shown in Figure 14.

$$\begin{cases} n_{\text{air}} \cdot \sin(\theta_{\text{air}}) & = n_{\text{prism}} \cdot \sin(\theta_{\text{prism}}) \\ n_{\text{prism}} \cdot \sin(60^\circ - \theta_{\text{prism}}) & = n_{\text{vapor}} \cdot \sin(\theta_{\text{vapor}}) \end{cases} \tag{10a}$$

$$\Rightarrow \begin{cases} n_{\text{air}} \cdot \sin(\theta_{\text{air,corrected}}) & = n'_{\text{prism}} \cdot \sin(\theta'_{\text{prism}}) \\ n'_{\text{prism}} \cdot \sin(60^\circ - \theta'_{\text{prism}}) & = n_{\text{vapor}} \cdot \sin(\theta_{\text{vapor}}) \end{cases} \tag{10b}$$

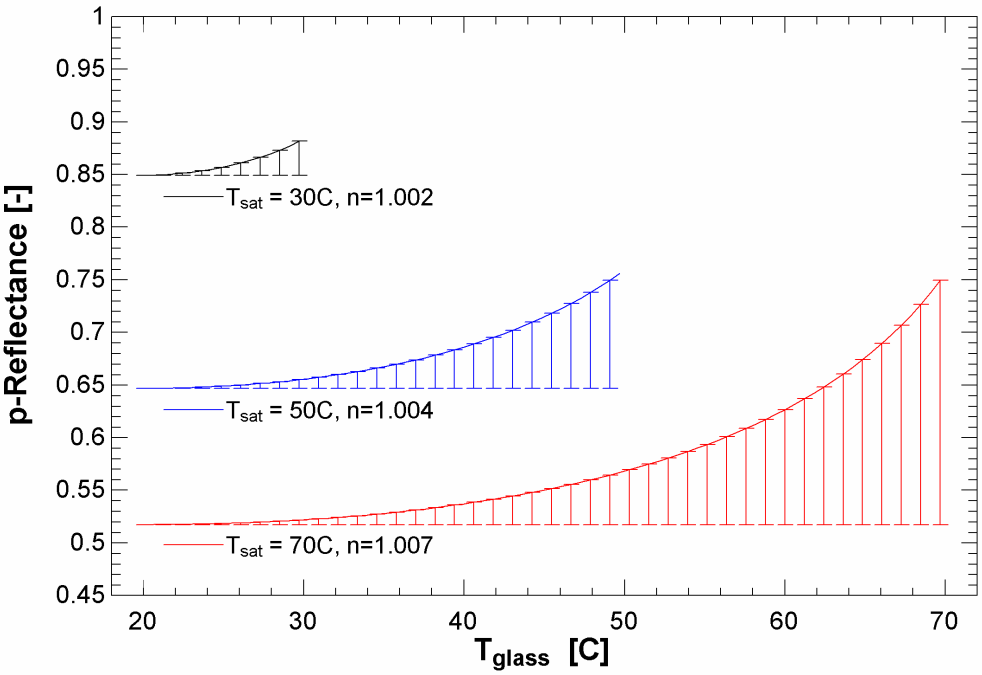

Figure 14: P-reflectance at the glass-vapor interface vs. prism temperature at three saturated vapor temperatures. An ideal TR setup would indicate constant reflectance values for saturated vapors at constant temperatures. Compared to their expected constant values, the three curves show as much as 80% error, which can be accounted for by $\theta_{\text{air,corrected}}$.

While Figure 14 shows the error in reflectance for various constant saturated vapor temperatures, such conditions are uncommon in the calibration process. Instead, the glass and prism temperatures both change with the vapor temperature. Figure 15 illustrates the case where the optical components maintain isothermal with the saturated vapor temperature at the glass wall. In this figure, the uncorrected curve shows the measured reflectance when the prism temperature equals the vapor temperature. The correction made with the corrected incident angle is shown as the the corrected curve. Through this process, the effects of the changing prism temperature can be accounted for without requiring an extensive calibration, mapping the reflectance, vapor density and prism temperature.

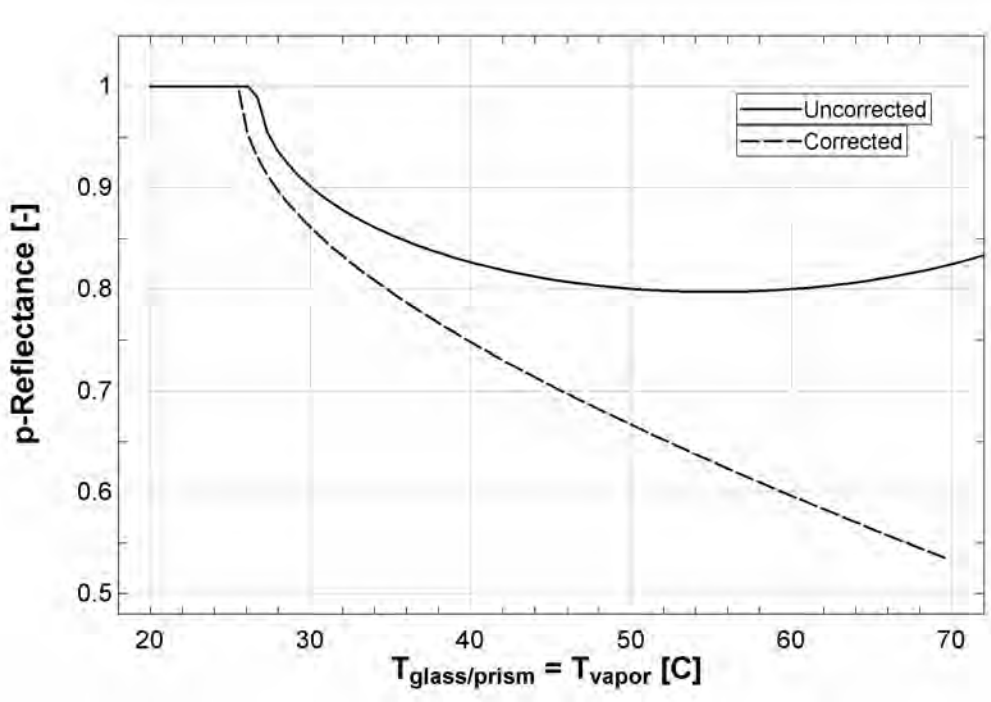

Figure 15: P-reflectance at the glass-vapor interface vs. isothermal saturated vapor and prism temperatures, plotted with and without adjustment for the changing glass/prism temperature. This figure demonstrates the worst case scenario of error in measuring vapor temperature.

2.3 Calibration Process

Due to imperfections inherent to all optical elements, a theoretical model alone is insufficient for carrying out reliable and accurate measurements. A calibration needs to be performed before a TR setup can be used for experimental measurements. The vapor TR calibration process is considerably more complicated than the liquid TR process due to the compressibility of vapor. A two-phase flow can be used in the liquid TR calibration process. The refractive index of the liquid film can be controlled simply by changing the liquid temperature upstream of the test section. Since the liquid at the wall can only exist at saturated conditions, no additional measurements need to be carried out, as the pressure is fixed. When vapor flows at the wall, however, it can be either saturated or superheated. Therefore, for the vapor calibration, controlling only the vapor temperature is insufficient. A single-phase flow is required for collecting calibration data for the vapor TR.

2.3.1 Single-Phase Calibration

For the vapor TR calibration, the pressure and temperature of superheated vapor flow are measured and used to calculate the vapor density with an equation of state [9]. Since pressure affects the vapor density more than temperature does within the range of relevant conditions, the slower response rate of the thermocouple relative to that of the pressure transducer was acceptable. This assumption was verified using the uncertainty propagation feature of Engineering Equation Solver (EES), where the temperature contributes at most 21% of the uncertainty in density. This occurs near the vapor saturation line at 210 kPa and 36°C. The overall uncertainty in density is shown in Figure 16 as a function of temperature and pressure. Using this process, the vapor intensity ratio is plotted with respect to the calculated density, as shown in Figure 17. This calibration measures the density using the TR method. With the test section pressure and vapor

density at the wall, the wall-vapor temperature is inferred assuming a uniform pressure.

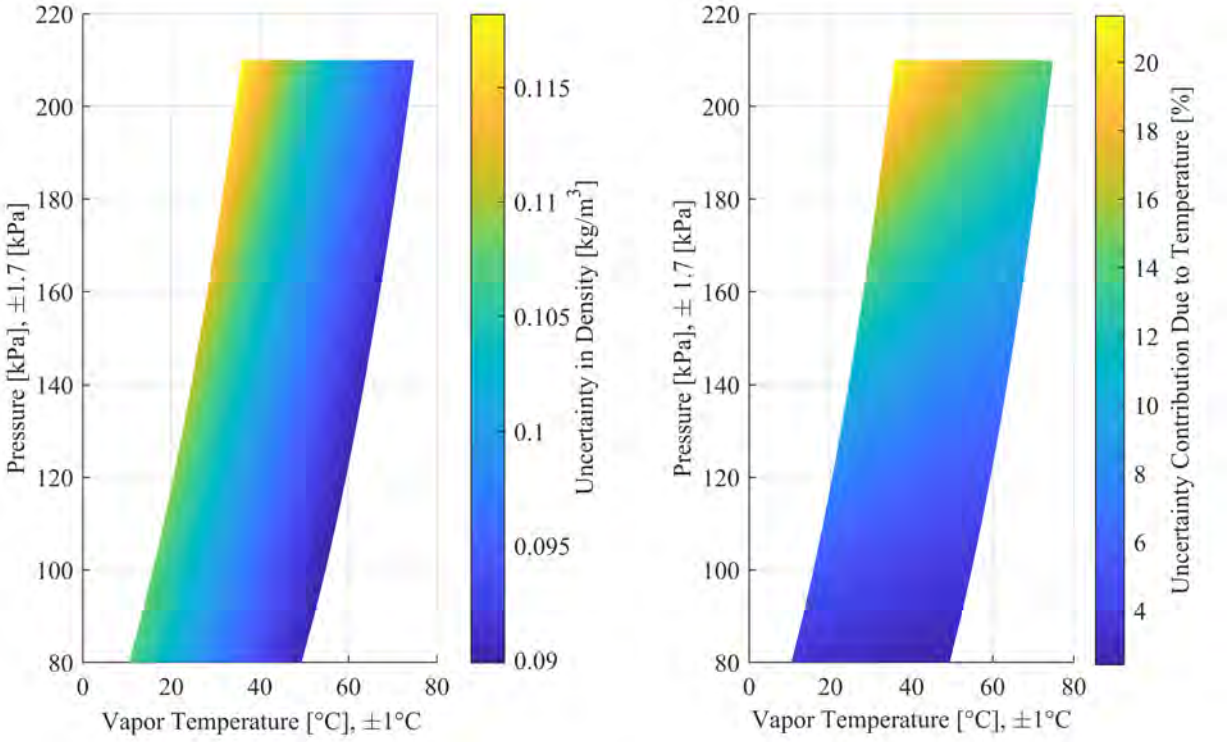

Figure 16: The left plot shows a 2D map of the propagated uncertainty in superheated (1 to 40°C) R245fa vapor density as a function of pressure and temperature. At pressure transducer and thermocouple uncertainties of 1.7 kPa and 1 K, the maximum uncertainty of 0.11 kg/m^3 occurs at a higher pressure, near the vapor saturation line (top-left corner). The right plot shows the percent contribution of uncertainty from the thermocouple measurement.

Using this calibration process, the 95% confidence interval of measured density is ±0.015 kg/m^3 for the mean density measurement[2]. The intensity ratio data were first discretized into 100 bins. Then, the confidence interval for each bin was calculated, assuming a normal distribution. These statistics can be seen in Figure 18 and 19. Finally, a polynomial curve fit was applied to describe the density as a function of intensity ratio. The curve fit is displayed in Figure 20.

[2]This value differs from that reported in Figure 16. The figure refers to the analytical uncertainty propagation using published sensor uncertainties. The calibration process calculates the uncertainty using the confidence interval of an oversampled dataset.

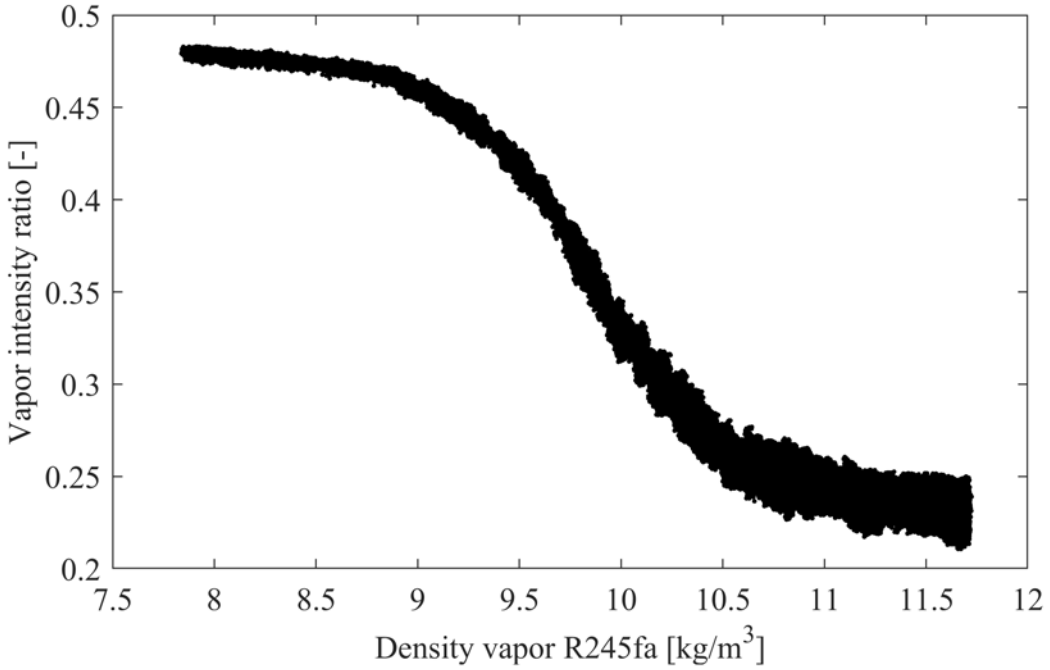

Figure 17: Intensity ratio versus density of vapor R245fa.

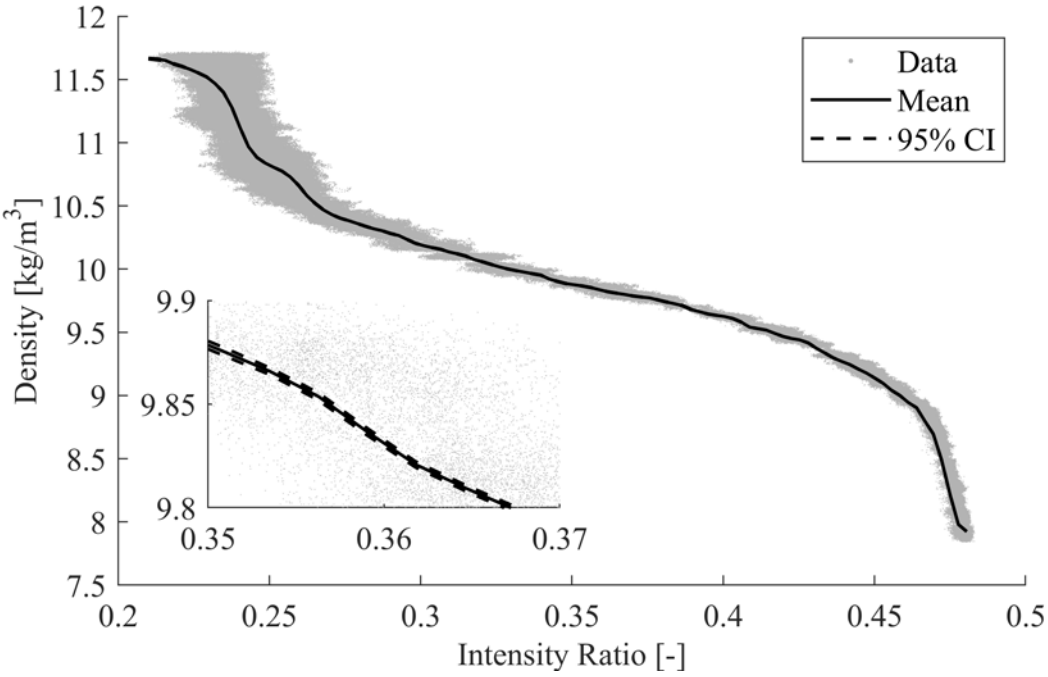

Figure 18: The 95% confidence interval of the density by intensity ratio is ± 0.015 kg/m^3. The narrow confidence interval near the ends is due to the large sample size in that region and the random noise distorting the normal distribution assumption. That is, the samples in bins near the two ends are not normally distributed.

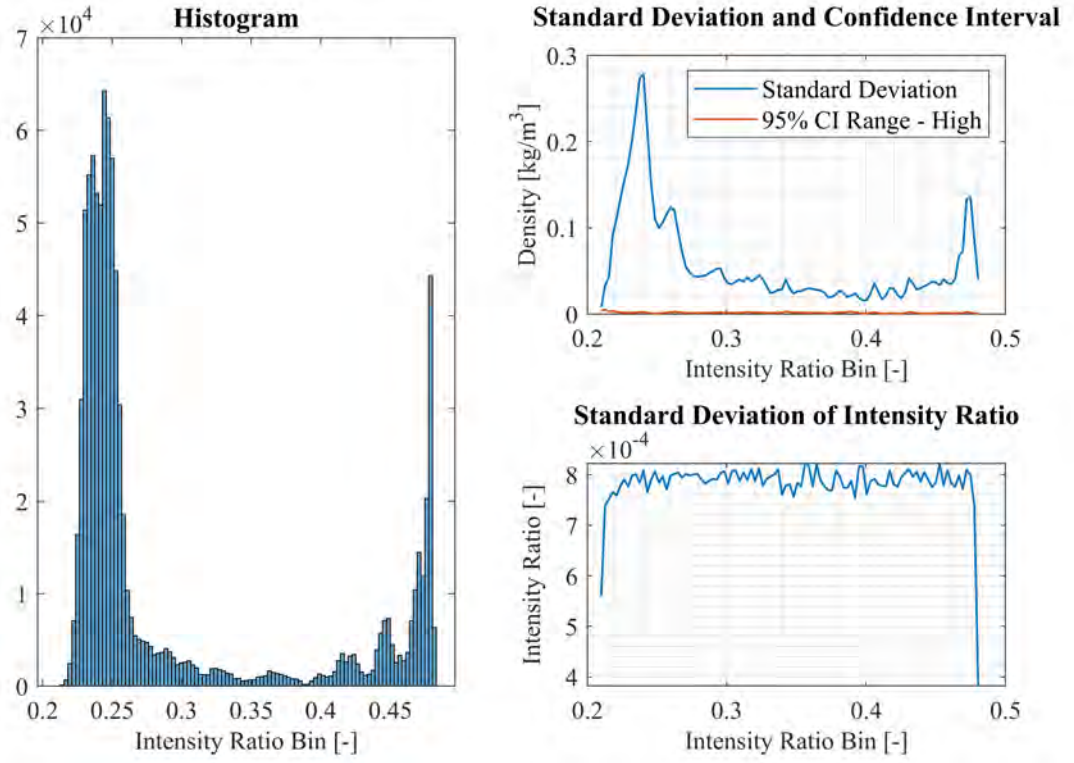

Figure 19: The density data ($\bar{s}_\rho = 0.0586$ kg/m^3) was discretized by intensity ratio ($\bar{s}_{ir} = 7.831\text{e}-4$) into 100 bins that are sufficiently populated (>100) to assume nearly normal distributions for z- scores to be used appropriately.

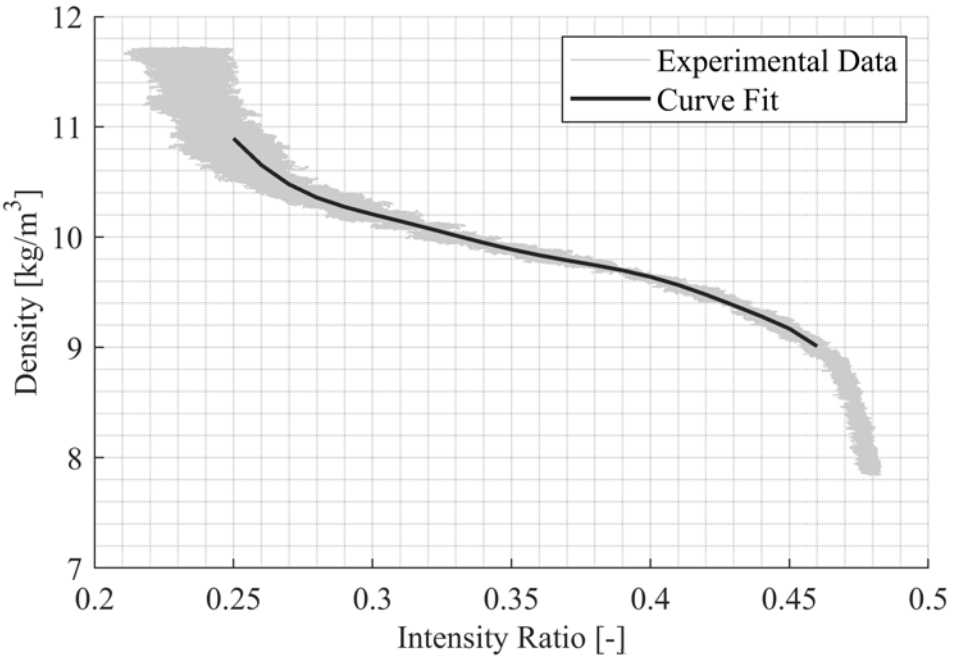

Figure 20: An example of the vapor density-intensity ratio calibration curve. The external wall temperature corresponding to the curve fit ranges from 32 to 36°C.

2.4 Heat transfer

The heat transfer coefficient (HTC) was inferred using a numerical model that includes the transient behavior of the wall, as shown in Figure 21. Both the liquid and vapor TR setups were used to collect this data. The vapor calibration curve in Figure 20 is only valid for the experimental data within the time from 30 to 110 seconds in the time trace, when the external window temperature ranged from 32 to 36°C. The jump in the external temperature at t=55 to 65 seconds is due to manual adjustments in the provided overall heat flux. To better illustrate the relationship between the two phase temperatures, the portion of data from t=100 to 104 seconds is shown in Figure 22.

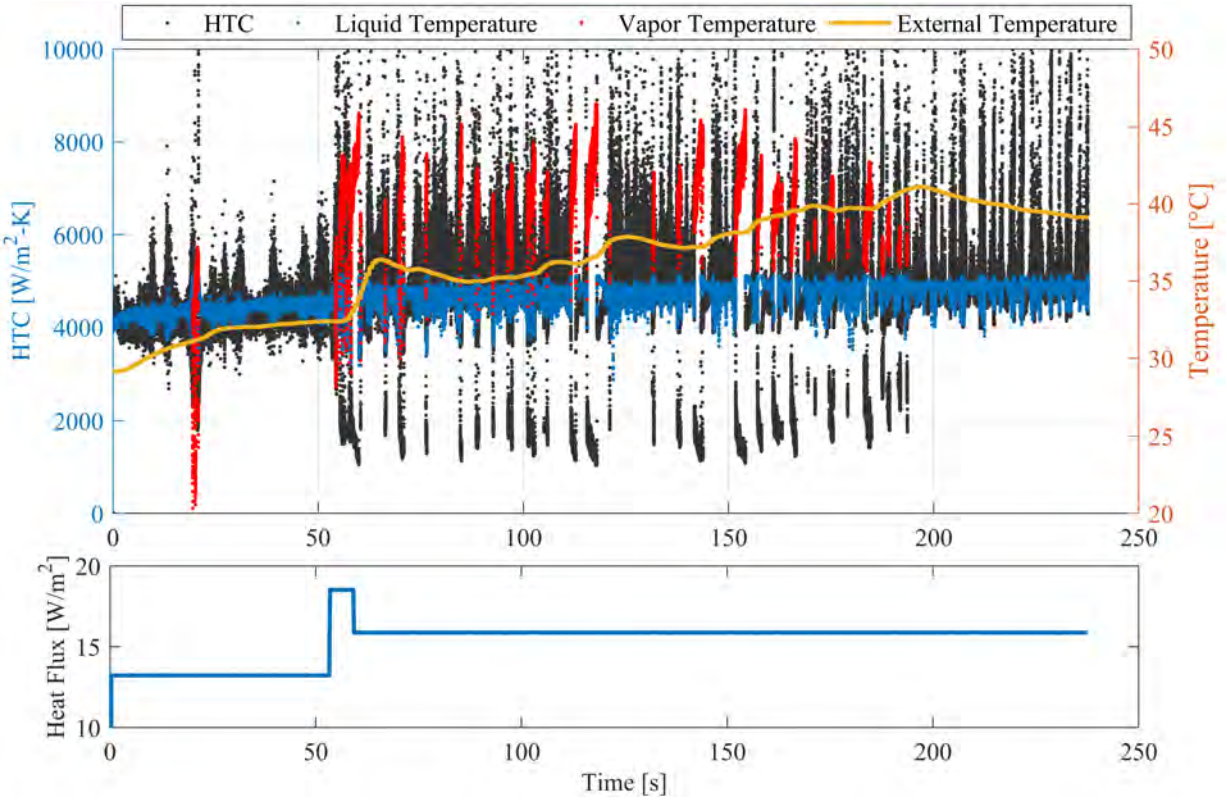

Figure 21: Instantaneous heat transfer coefficient with liquid, vapor, and external wall temperatures overlaid. Both the liquid and vapor TR setups were used to collect this data.

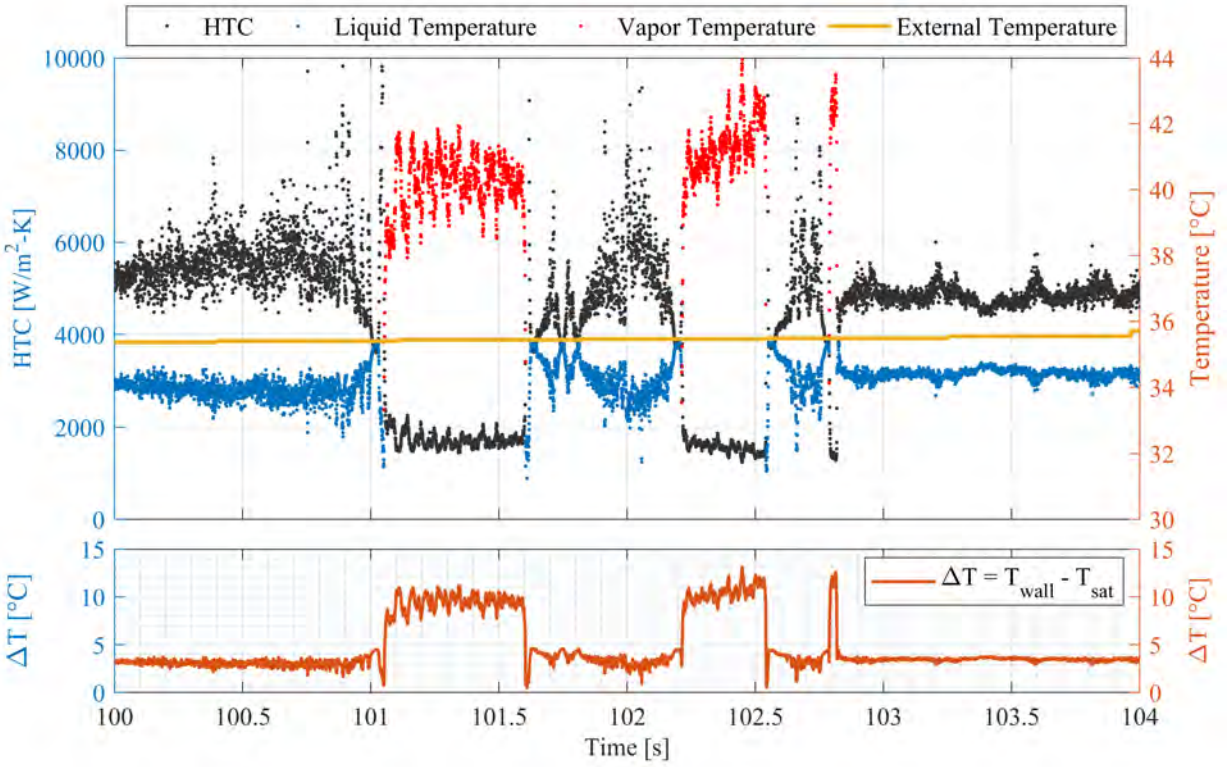

Figure 22: The HTC and wall temperature of cyclic re-wetting events over a 4 second period at a nearly constant external window temperature shows the potential of the vapor TR setup.

As seen in Figure 22, small changes in the wall-liquid temperature (±1°C) correspond to large fluctuations in the liquid HTC (±1500-2000 W/m^2-K), whereas slightly larger changes in the wall-vapor temperature (±2°C) yield smaller changes in the vapor HTC (±500 W/m^2-K). Newton's law of cooling relates the change in wall-fluid temperature (T_{wall}) to the change in the HTC (h), for some heat flux, $\dot{q}''$, and bulk temperature, T_∞. The error in the HTC is related to the error in T_{wall}.

$$\begin{aligned} \frac{\partial h}{h} &= -\frac{\partial T_{wall}}{T_{wall} - T_\infty} \\ \Rightarrow \partial h &= -\frac{\partial T_{wall}}{(T_{wall} - T_\infty)^2} \cdot \dot{q}'' \end{aligned} \tag{11}$$

For a constant heat flux, since the temperature difference ($\Delta T = T_{wall} - T_\infty$) is larger for

vapor convection than for liquid convection, small changes in the wall-vapor temperature yield smaller changes in the vapor HTC.

For the experimental conditions under which the data in Figure 22 were collected, where the fluid saturation temperature is 30°C and the wall heat flux is approximately 16 kW/m^2, by Equation (11), a 2°C error in the wall-liquid temperature yields a 2000 W/m^2-K error in the liquid HTC. The same error in the wall-vapor temperature yields a 320 W/m^2-K error in the vapor HTC. In other words, similar absolute uncertainties in the HTCs can be achieved for both TR setups even with higher uncertainties in the wall-vapor temperature measurements. Using measured test section conditions, the Dittus-Boelter equation for estimating the HTC in a developed vapor flow underestimated the vapor HTC by about a factor of 5. This is shown in Figure 23. Nominal values of the test section conditions are displayed in Table 2. Several untested theories to explain this discrepancy follow:

Table 2: Nominal test section conditions

Parameter	Value	Unit
G_g	130.00	kg/s-m^2
G_l	12.00	kg/s-m^2
Re_g	1.93E5	-
Re_l	5.85E2	-
Pr_g	0.68	-
Pr_l	5.44	-
k_g	0.0163	W/m-K
k_l	0.0903	W/m-K

- Developing flow: The Dittus-Boelter equation assumes a turbulent single-phase flow with a development length of at least 10 hydraulic diameters. Both assumptions cannot be made for the short-lived (and sometimes partial) cyclic dryouts that were observed in the data shown in Figures 21 and 23. Comparing the Dittus-Boelter model with experimental data for sustained dry-outs, where the two-phase annular flow transitions into a fully developed single-phase vapor flow, may help explain

this discrepancy.

- Span-wise heat transfer: Due to the higher HTC associated with the liquid film compared to that of vapor, during a partial dry-out, span-wise heat transfer can occur from the dried-out area to the wet area, effectively lowering the wall-vapor temperature compared to that of a single-phase vapor flow. This can cause an overestimation of the vapor HTC from the measured data. More simultaneous measurements of TR data and wet fraction images are needed to validate this theory.

- Temperature cutoff: The wall-vapor temperature may rise past the temperature cutoff of the vapor TR setup, beyond which no measurement sensitivity remains. Near-instant spikes in the wall-vapor temperature data could either be physical or due to measurements beyond the temperature cutoff. While this type of cutoff was not evident in this data set, the short rise-time of the wall-vapor temperature as shown in Figure 23 needs to be further investigated.

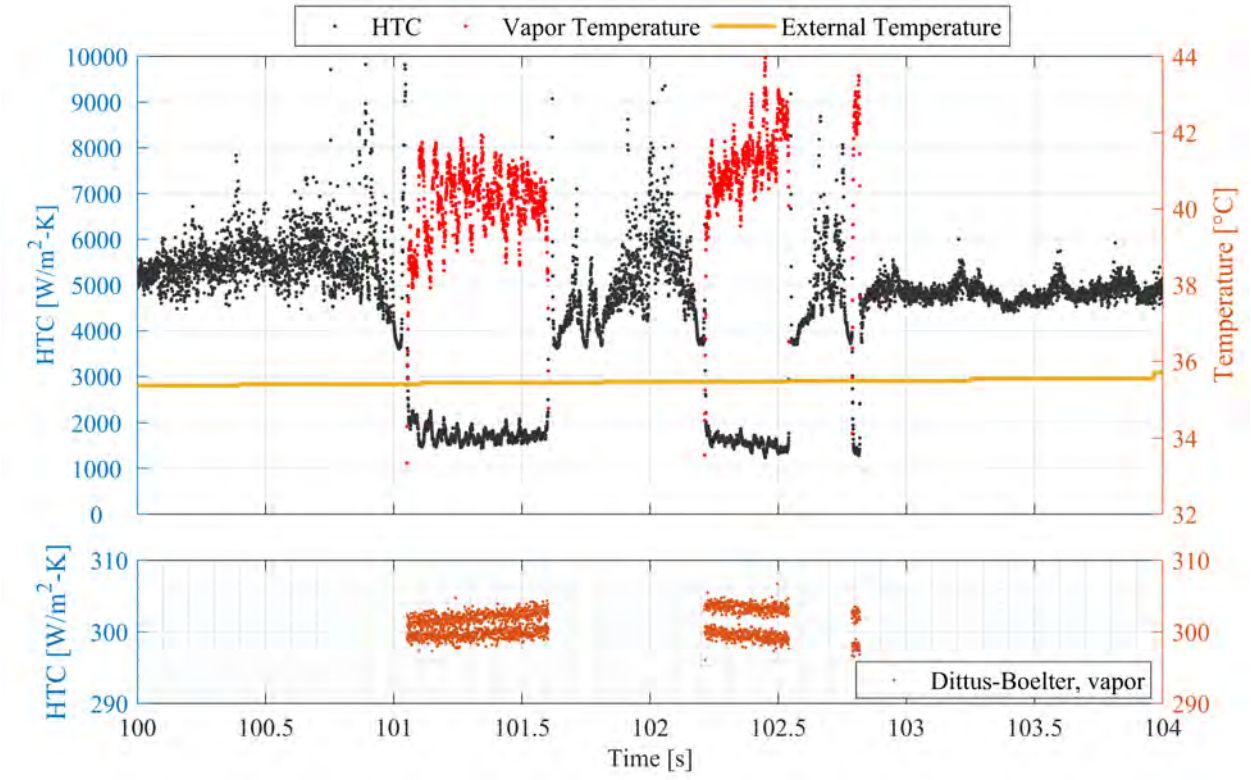

Figure 23: The Dittus-Boelter heat transfer coefficients underestimate the transient values calculated from experimental data by a factor of five. Three theories for explaining this discrepancy are proposed.

3 Refractometer

R245fa, the working fluid of the annular flow facility, is used in a wide variety of closed-cell spray polyurethane foam systems [5]. Since the optical properties of the fluid are unlikely to be important when the fluid is used as a blowing agent, publication of its refractive index as a function of temperature and pressure is unavailable except for one by Schmidt et al. [14]. Schmidt et al. published the refractive index of both saturated liquid and vapor R245fa from room temperature to the critical point. While the liquid data is sufficient for making liquid TR measurements, vapor data at only saturated conditions is not as useful in modeling vapor TR calibration curves. Further, the published data contained only five data points between 20 and 100°C—the temperature range of experimental interest. Of the five, only two are relevant for the operating pressure range of the test section. While the Lorentz-Lorenz, equation (2) was used to curve fit the published experimental data as a function of vapor density, independent measurement of the vapor refractive index was collected to verify the TR model.

3.1 Optical theory

Countless refractometry methods have been published and produce similar results. For the convenience of using existing equipment, an optical method that measures the critical angle was used. The original work by Hurlburt and Newell [6] used this optical technique to measure the thickness of liquid thin films. The theory is similar to that of the thermoreflectance technique, where the reflectance of a light ray propagating from a denser medium to a rarer medium depends on the incident angle relative to the critical angle. Figure 24 illustrates the optical setup for the refractometer. First, a laser beam is directed perpendicular to a transparent glass window. The incident ray is then dispersed by a white tape on the incident glass surface. The dispersed ray then propagates towards the FTO and the R245fa vapor. At the FTO-vapor interface, light rays propagating

below the critical angle are partially transmitted, while those propagating at and above the critical angle are reflected. Since the transmitted rays at the FTO-vapor interface are closer to the initial incident laser beam than the reflected rays, a dark area can be observed in the center. Consequently, a light ring is observed. The diameter of the light ring is calculated

$$D = 4[\tan(\theta)h_{window} + \tan(\theta_c)h_{FTO}] \tag{12}$$

where θ is the incident angle at the window-FTO interface, θ_c is the critical angle at the FTO-vapor interface, h_{FTO} is the thickness of the FTO, and h_{window} is the glass window thickness. The two angles (θ and θ_c) are defined by Equation (4) and are functions of the materials' refractive indices. By measuring the diameter of the projected light ring, the vapor refractive index is calculated, assuming all else remain constant.

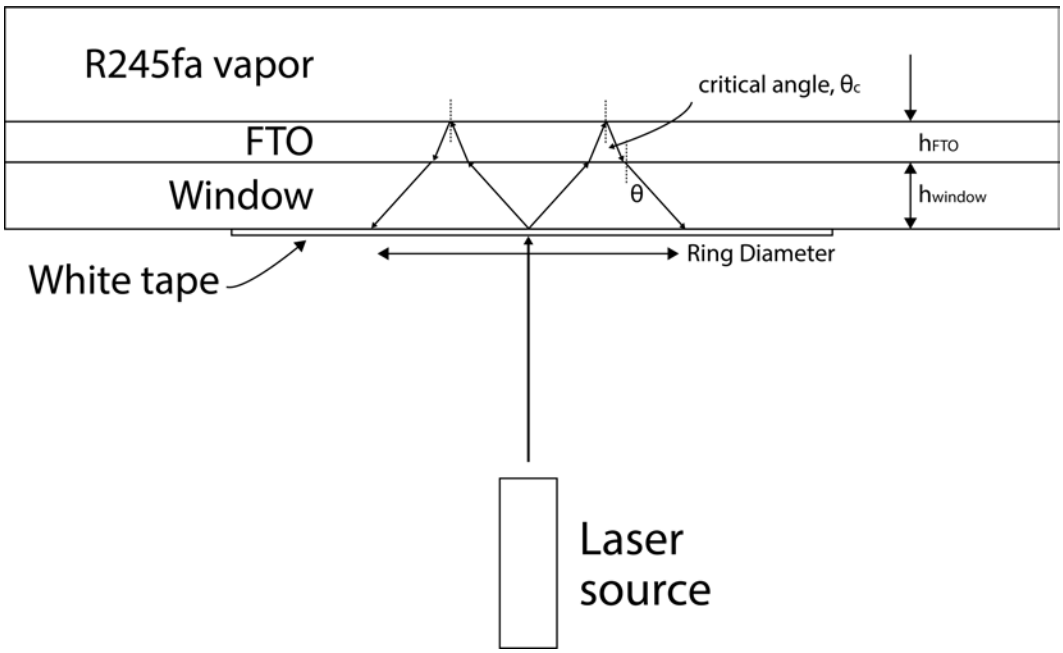

Figure 24: Illustration of the optical setup for the refractometer. Not to scale.

If rays approaching at less than the critical angle are completely transmitted, and the rays at and above the critical angle are completely reflected, a sharp boundary is formed by the reflection of the rays that propagate at the critical angle. However, this

is not the case according to Equation (3). Figure 25 shows that the reflectance of a beam propagating at an angle below the critical angle is not only finite but increases as it approaches the critical angle, regardless of the beam polarization. This increasing reflectance results in a less-defined border for the projected light ring and is more difficult to detect. A sample image is shown in Figure 26.

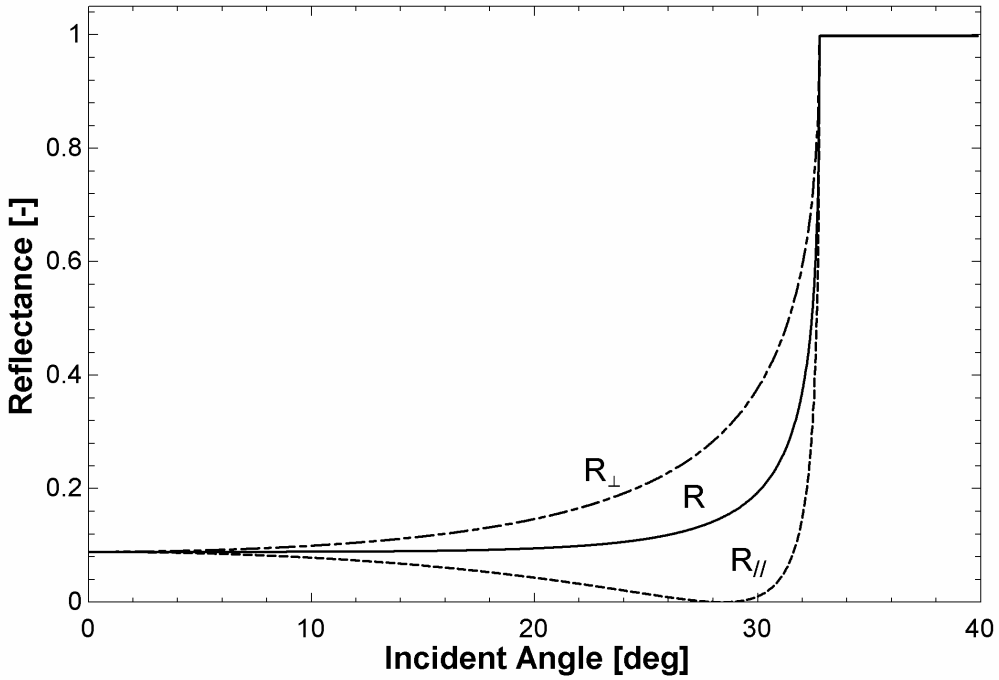

Figure 25: Reflectance at the FTO-vapor interface of s-polarized ($R_{\perp}$), evenly polarized (R), and p-polarized ($R_{//}$) beams. The steady increase in reflectance of a beam before the critical angle leads to a less defined light ring.

3.2 Experimental setup

The optical setup for this refractometer involves only a few components. From left to right in Figure 27, a 632.8 nm HeNe laser is directed normal to the glass window of a vapor cell. The white tape on the window diffuses the beam and serves as a projection screen for the reflected image. This image is captured on a CMOS camera (Basler #acA2000-

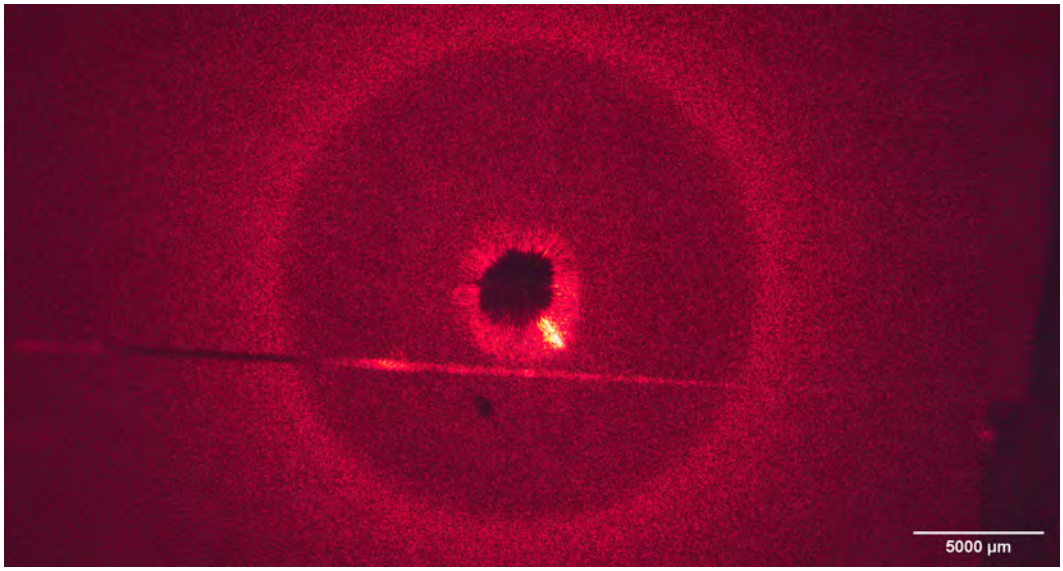

Figure 26: Light ring caused by the critical angle. As light rays propagate to the FTO-vapor interface, some are reflected and some are transmitted. Incident rays that are close to and above the critical angle are reflected and create a light ring.

165um) with a zoom lens (Thorlabs #MVL12X3Z). Since the incident laser beam and the reflected image share the same optical axis, a turning mirror with an on-axis through hole is used. An illustration of the window is shown in Figure 28. The through-hole allows the incident beam to pass through while the mirror allows the reflected image to be captured on a camera. The diameter of the ring is measured by curve-fitting a circle on the ring in the captured image.

The temperature and pressure of the vapor in the vapor cell (Figure 29) is controlled through the built-in heat exchange coil (shown in brown). A water-propylene-glycol mixture circulates through the copper coil from a cooling/heating water bath. The cell vapor temperature is controlled by changing the water bath setpoint. Pressure control is achieved by changing the amount of fluid in the vapor cell. Thermocouples and a pressure transducer are connected to the vapor cell on the side access ports.

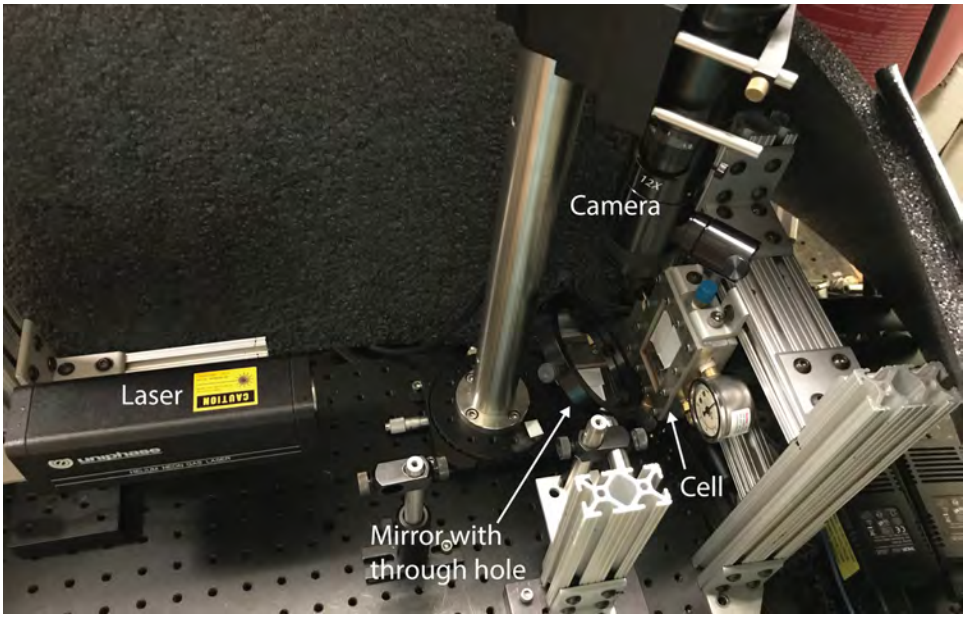

Figure 27: Refractometer setup. The laser beam passes through a hole in the mirror before reaching the diffusing white tape on the test cell. The reflected image on the window is captured by the camera using the mirror.

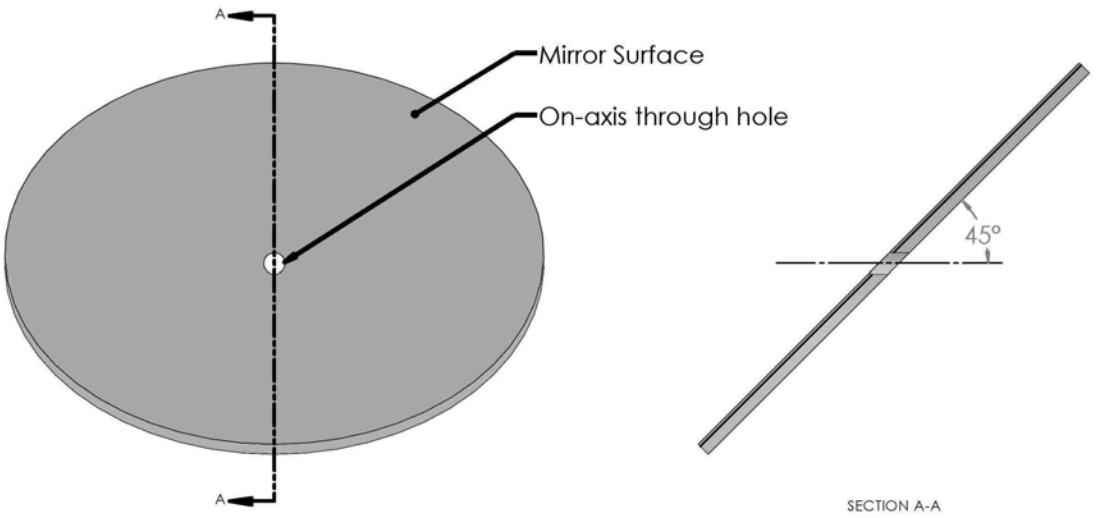

Figure 28: Turning mirror with an on-axis through hole. The through-hole allows the incident beam to pass through, while the mirror allows the reflected image to be captured by a camera.

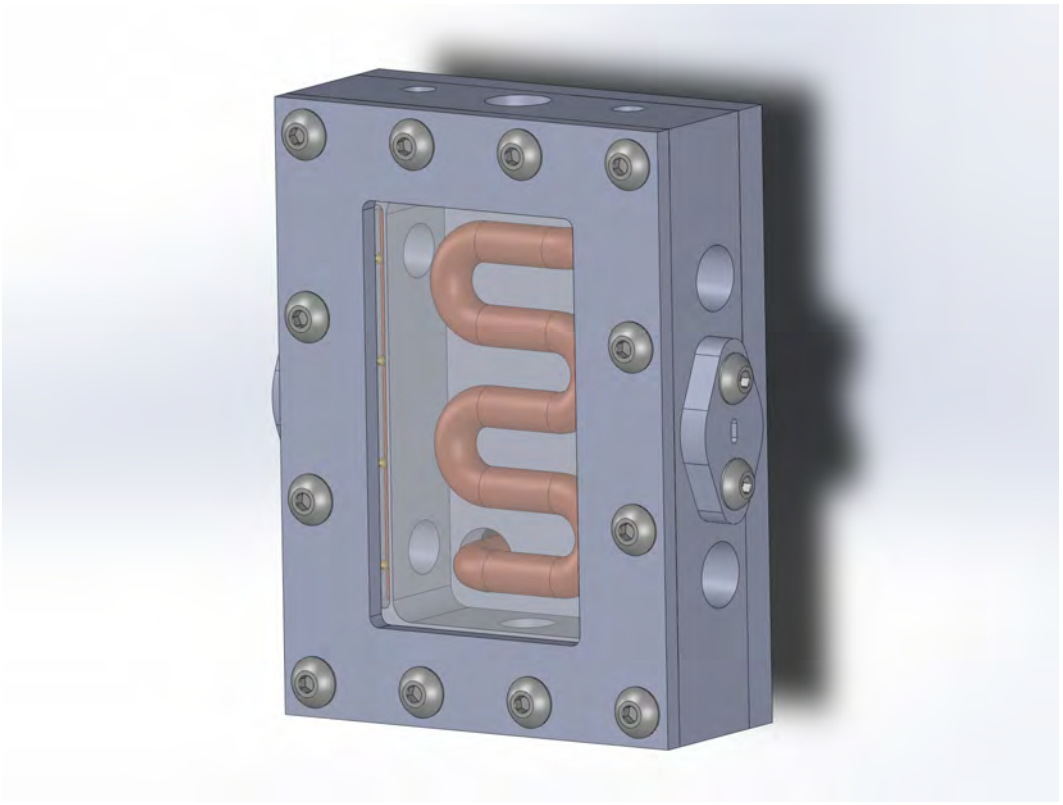

Figure 29: Refractometer vapor cell. The cell temperature was controlled by a water-propylene-glycol mixture circulated through the copper coil from a temperature-controlled water bath.

3.3 Calibration Results

The refractive index of the glass window, n_{window}, is first measured by filling the cell with air (n=1.00027), a fluid with a well-known refractive index. The refractive index of the glass window is determined to be 1.521. The refractometer is then validated by measuring the refractive index of liquid 2-propanol (LabChem #LC157502, purity $\geq$ 99.5%)—another fluid with well-documented properties. Measurements of the refractive index are made at various temperatures from 10°C to 45°C and compared to the published data by O'Brien and Quon [10] in Figure 30. By comparing their respective best-fit-curve, it is evident that the measured data is offset by a constant of $\Delta n = 0.021$. This constant offset suggests the optical setup is valid, but the parameters used, such as the window thickness, may be inaccurate, leading to a systematic error.

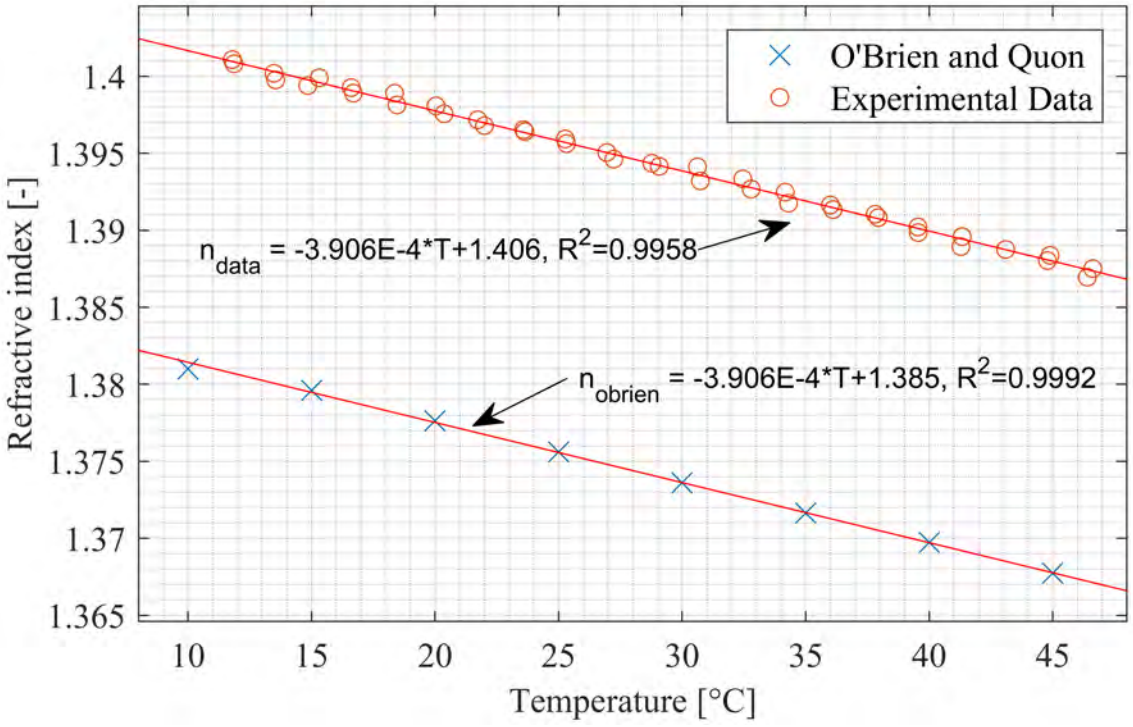

Figure 30: Refractive index (n) of 2-propanol. The constant offset between the measured and published data suggests an error in the window thickness or refractive index.

The source of this mismatch is investigated by analyzing the associated equations.

First, expressions of θ and θ_c as functions of the materials' refractive indices by Equation (4) are substituted into Equation (12)

$$D = 4\big[\tan(\arcsin\frac{n}{n_{window}})h_{window} + \tan(\arcsin\frac{n}{n_{FTO}})h_{FTO}\big], n = n(T) \tag{13}$$

where n, n_{window}, and n_{FTO} are refractive indices of the fluid, window and FTO respectively. The fluid refractive index, n, is a function of temperature, T, as is the case with most liquids. Since h_{FTO} is on the order of 10 nm, while h_{window} is 3.00±0.01 mm, the FTO layer contributes minimally to the ring diameter, D. Therefore, (13) can be simplified to

$$D = 4\big[\tan(\arcsin\frac{n(T)}{n_{window}})h_{window}\big] \tag{14}$$

and solved for n,

$$n = \sin\Big[\arctan(\frac{D}{4h_{window}})\Big] \cdot n_{window} \tag{15}$$

The relative change in n with respect to change in h_{window} and n_{window} can be expressed by

$$\frac{\Delta n}{n} = \Delta h_{window} \cdot \frac{-16 \cdot h_{window}}{D^2 + 16h_{window}^2} \tag{16}$$

$$\frac{\Delta n}{n} = \frac{\Delta n_{window}}{n_{window}} \tag{17}$$

Using the rated uncertainty of 0.01 mm for the window thickness measurement (Δh_{window}), Equation (16) shows that at D=10 mm, the uncertainty of the measured vapor refractive index (Δn) is ±0.001. This is an order of magnitude smaller than the calculated offset (0.021). On the other hand, evaluating (17) with $\Delta n = 0.021$, $n = 1.406$, and $n_{window} = 1.521$, the window refractive index needs to be adjusted from $\Delta n_{window} = 0.0227$ to 1.5437 to correct the data. Using this offset, the previously shown data is reanalyzed and plotted in Figure 31. The measured data overlays the published data after applying this offset.

The same analysis is carried out with respect to the diameter, D,

$$\frac{\Delta n}{n} = \Delta D \cdot \frac{16 \cdot h_{window}^2}{D^3 + 16 D h_{window}^2} \tag{18}$$

to show the relative change in n as a function of ΔD. This time, using $\Delta n = 0.021$, $n = 1.375$ (published data at 25°C), $h_{window} = 3$ mm, and $D = 25.94$ mm (from Equation (15)), ΔD evaluates to 2.247 mm, an 8.7% error.

Clearly, several sources of error can be attributed to the offset in Figure 30. Moreover, the sources of error are not mutually exclusive. The need for an additional offset for the measurements to match published data shows further work is needed before this refractometry method can be used on a fluid with an unknown refractive index.

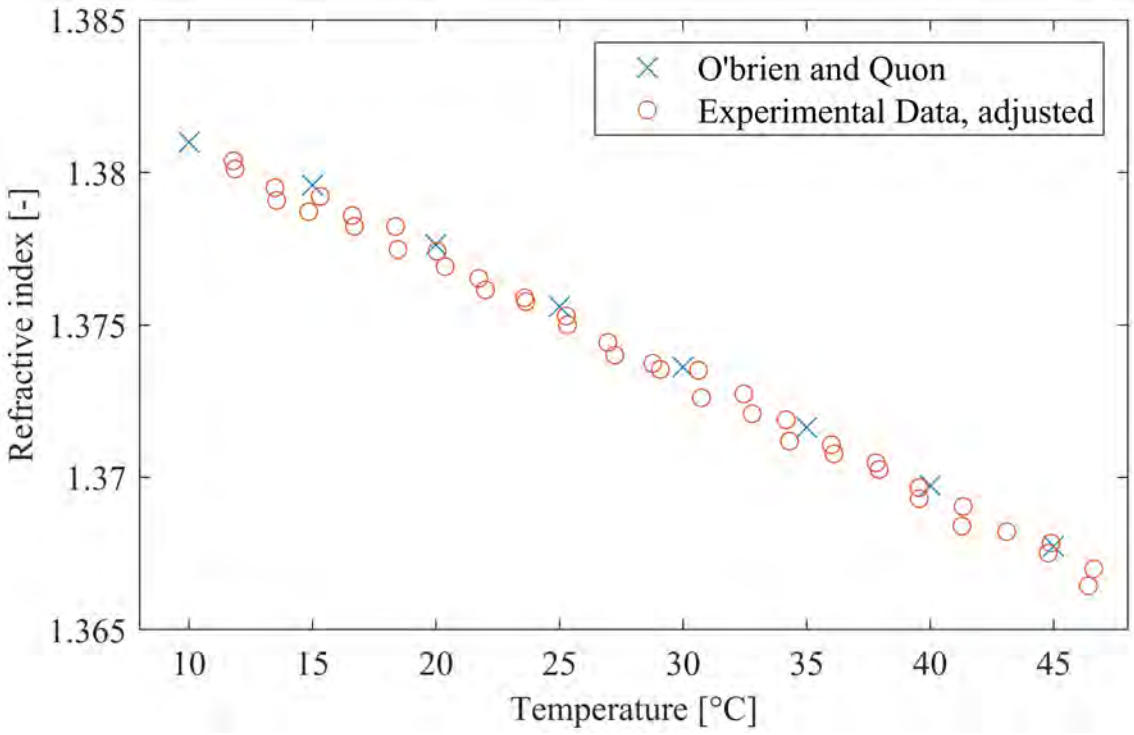

Figure 31: Adjusted refractive index (n) of 2-propanol.

3.4 Future Work

Currently, the light ring diameters have been measured by fitting a circle on the captured images. The curve fitting algorithm defines the boundary as the radial point from the center with the greatest pixel-value gradient. This definition is consistent between data points but not with respect to literature. That is, the slope of the curve matches that in literature, but the values are offset. The cause of this offset needs to be resolved. From the example shown in Figure 26, the boundary defining the light ring is not obvious even by eye. Two methods for improving the ring detection accuracy have been proposed.

First, the finite beam width of the incident laser light leads to a finite ring boundary width. In Figure 24 in the optical theory section, a point source is used to illustrate the diffused beam at the white tape. If the reflectance behaved as a step function, the ring boundary would be a well-defined curve. This, however, is not the case. Figure 32 shows a modified version with an incident beam of finite diameter that results in a reflected light ring with a border of finite width. The offset error in ring diameter, calculated using Equation (18), is on the same order of magnitude as the incident beam. This, in addition to the effects of the "ramping reflectance" results in an ambiguous boundary. The obvious solution here, then, is to minimize the beam diameter. Another solution is to use a moderately thick glass. The thicker the window, the larger the projected light ring, and a larger change in the diameter per unit change in fluid refractive index. The thickness can only be increased moderately as the power density of the reflected beam decreases with increasing thickness, leading to a progressively dimmer projection.

Second, a p-polarized beam may be preferred for enhancing the ring boundary. As shown in Figure 25, the reflectance of an s-polarized beam increases more gradually than that of a p-polarized beam does. In fact, the Brewster's angle just before the critical angle should result in a dark patch on the projection when a p-polarized beam is used.

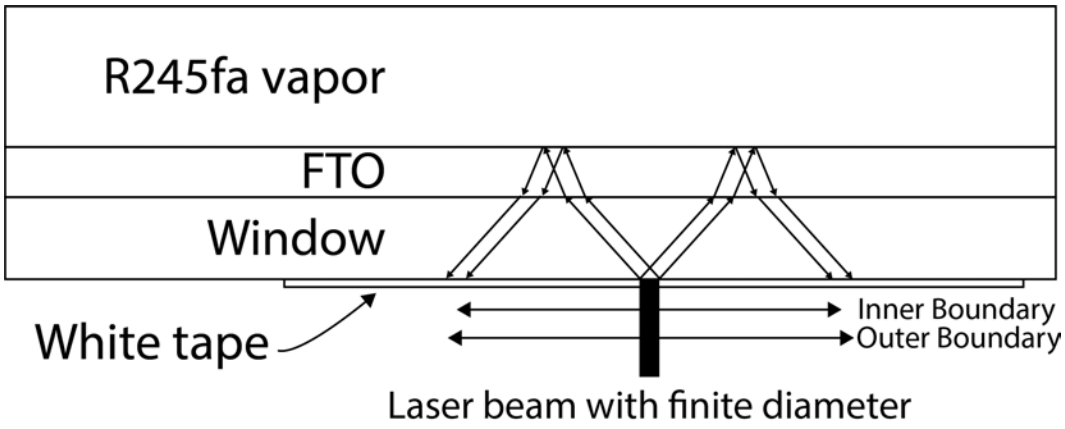

Figure 32: Effects of a finite incident beam diameter. Not to scale.

The current experimental setup uses a randomly polarized[3] HeNe laser source, which could lead to a less well-defined boundary.

[3]The output beam polarization of a randomly polarized laser source changes with time, while that of a linearly polarized one does not.

4 Conclusion

A wall-vapor temperature measurement technique was designed and implemented. A calibration procedure was developed, and the technique was used to calculate the heat transfer coefficient associated with an annular flow under cyclic re-wetting conditions. Comparison of the measured heat transfer coefficient with literature shows the technique needs to be further validated and more work is needed to characterize the heat transfer at the wall.

A refractometer was designed and built to record more accurate measurements of the R245fa vapor refractive index as a function of pressure and temperature. Validation using 2-propanol shows deficiencies with the current optical setup. Methods for improvement were discussed.

References

[1] Max Born, Emil Wolf, A. B. Bhatia, P. C. Clemmow, D. Gabor, A. R. Stokes, A. M. Taylor, P. A. Wayman, and W. L. Wilcock. *Principles of Optics*. Cambridge University Press, Oct 1999. doi: 10.1017/cbo9781139644181. URL http://dx.doi.org/10.1017/CBO9781139644181.

[2] Matteo Bucci, Andrew Richenderfer, Guan-Yu Su, Thomas McKrell, and Jacopo Buongiorno. A mechanistic ir calibration technique for boiling heat transfer investigations. *International Journal of Multiphase Flow*, 83:115 – 127, 2016. ISSN 0301-9322. doi: https://doi.org/10.1016/j.ijmultiphaseflow.2016.03.007. URL http://www.sciencedirect.com/science/article/pii/S030193221530183X.

[3] Philip E. Ciddor. Refractive index of air: new equations for the visible and near infrared. *Appl. Opt.*, 35(9):1566–1573, Mar 1996. doi: 10.1364/AO.35.001566. URL http://ao.osa.org/abstract.cfm?URI=ao-35-9-1566.

[4] B.E. Fehring, R.W. Morse, J. Chan, K.M. Dressler, E.T. Hurlburt, G.F. Nellis, and A. Berson. Instantaneous optical measurement of the temperature at the interface between a wall and a thin liquid film. *Measurement Science and Technology - Optical and Laser-Based Techniques*, 2020. (to appear).

[5] Honeywell. Honeywell foam blowing agents features and benefits. URL https://www.fluorineproducts-honeywell.com/blowingagents/wp-content/uploads/2017/07/honeywell-solstice-lba-enovate-brochure.pdf.

[6] E. T. Hurlburt and T. A. Newell. Optical measurement of liquid film thickness and wave velocity in liquid film flows. *Experiments in Fluids*, 21(5):357–362, September 1996. doi: 10.1007/bf00189056. URL https://doi.org/10.1007/bf00189056.

[7] Hyungdae Kim, Youngjae Park, and Jacopo Buongiorno. Measurement of wetted area fraction in subcooled pool boiling of water using infrared thermography. *Nuclear Engineering and Design*, 264:103 – 110, 2013. ISSN 0029-5493. doi: https://doi.org/10.1016/j.nucengdes.2013.07.002. URL http://www.sciencedirect.com/science/article/pii/S0029549313003233. SI:NURETH-14.

[8] Sung-Min Kim and Issam Mudawar. Universal approach to predicting saturated flow boiling heat transfer in mini/micro-channels (part ii) two-phase heat transfer coefficient. *International Journal of Heat and Mass Transfer*, 64:202–217, 2013.

[9] Eric W. Lemmon and Roland Span. Short fundamental equations of state for 20 industrial fluids. *Journal of Chemical & Engineering Data*, 51(3):785–850, 2006. doi: 10.1021/je050186n.

[10] Robert N. O'Brien and D. Quon. Refractive index of some alcohols and saturated hydrocarbons at 6328 a. *Journal of Chemical & Engineering Data*, 13(4):517–517, 1968. doi: 10.1021/je60039a017. URL https://doi.org/10.1021/je60039a017.

[11] Chetan K. Parmar, Garry Rumbles, and Christopher J. Winscom. Aggregation of azamethine dyes on hydrated glass surfaces: An evanescent wave-induced fluorescence study. *Phys. Chem. Chem. Phys.*, 4:1766–1775, 2002. doi: 10.1039/B108865C. URL http://dx.doi.org/10.1039/B108865C.

[12] Andrew Richenderfer, Artyom Kossolapov, Jee Hyun Seong, Giacomo Saccone, Etienne Demarly, Ravikishore Kommajosyula, Emilio Baglietto, Jacopo Buongiorno, and Matteo Bucci. Investigation of subcooled flow boiling and chf using high-resolution diagnostics. *Experimental Thermal and Fluid Science*, 99:35 – 58, 2018. ISSN 0894-1777. doi: https://doi.org/10.1016/j.expthermflusci.2018.07.017. URL http://www.sciencedirect.com/science/article/pii/S089417771831255X.

[13] Mark Arthur dissertant Rodarte. *Liquid film and droplet behavior in adiabatic and diabatic vertical annular flow.* [Madison, Wis.] : [University of Wisconsin–Madison], 2015., 2015. URL https://search.library.wisc.edu/catalog/9911143894002121. Advisor: Timothy Shedd.;Ph.D. University of Wisconsin–Madison 2015.;Includes bibliographical references (pages 303-317).

[14] James W Schmidt, Ernesto Carrillo-Nava, and Michael R Moldover. Partially halogenated hydrocarbons chfclcf3, cf3ch3, cf3chfchf2, cf3ch2cf3, chf2cf2ch2f, cf3ch2chf2, cf3ochf2: critical temperature, refractive indices, surface tension and estimates of liquid, vapor and critical densities. *Fluid Phase Equilibria*, 122(1):187 – 206, 1996. ISSN 0378-3812. doi: https://doi.org/10.1016/0378-3812(96)03044-0. URL http://www.sciencedirect.com/science/article/pii/0378381296030440.

[15] SCHOTT Advanced Optics. Temperature Coefficient of the Refractive Index TIE-19. 2016. URL https://www.schott.com/d/advanced{_}optics/3794eded-edd2-461d-aec5-0a1d2dc9c523/1.1/schott{_}tie-19{_}temperature{_}coefficient{_}of{_}refractive{_}index{_}eng.pdf.

[16] SCHOTT Advanced Optics. Optical Glass Data Sheets. 2019. URL https://www.schott.com/d/advanced{_}optics/ac85c64c-60a0-4113-a9df-23ee1be20428/1.14/schott-optical-glass-collection-datasheets-english-may-2019.pdf.

[17] Yury V. Semenyuk, Vitaly V. Sechenyh, Vitaly P. Zhelezny, and Pavel V. Skripov. Thermophysical properties of compressor oils for refrigerating plant. *Journal of Synthetic Lubrication*, 25(2):57–73, 2008. doi: 10.1002/jsl.50. URL https://onlinelibrary.wiley.com/doi/abs/10.1002/jsl.50.

[18] Timothy A Shedd and Benjamin W Anderson. An automated non-contact wall temperature measurement using thermoreflectance. *Measurement Science and Technology*, 16(12):2483–2488, Nov 2005. doi: 10.1088/0957-0233/16/12/012. URL https://doi.org/10.1088%2F0957-0233%2F16%2F12%2F012.

5 Appendix

5.1 LabVIEW Control Program Revision

The careful design of the control and data acquisition (DAQ) systems of the MFVAL annular flow facility is critical to its operation, equipment and operator safety, and experimental efficiency. This has been implemented in LabVIEW. Over the years of the facility's operation, the once sufficient LabVIEW programs became difficult to maintain due to their lack of expandability. The original LabVIEW programs were revised and integrated to address these issues.

The documentation of each LabVIEW VIs and subVIs has been embedded in the program itself. Use the "context help" function to access the full documentation. The following sections are meant to explain the overall framework structure and key functionalities that have been implemented.

5.1.1 Revision Principle

In the interest of future-proofing all long term computer programs today, provisions for expandability have become essential. This iteration of the revision focuses on modular programming. The four main modules and their respective submodules are listed below and explained in the next section.

1. Configuration
    - Sensor configuration
    - Input/Output configurations
    - Trigger thresholds for safety mechanisms
2. Validation and Initialization
    - Validate channel configuration
    - Initialize front panel control
    - Initialize data First-In, First-Out (FIFO) queue
3. Measurement Loop
    - Configure NI-DAQmx driver
    - Create input data structure
    - Continuously collect sensor data
    - Test section window heater control
    - Pulse generator control
    - Loop data visualization

- Loop data logging system
- Sensor offset management
- Liquid and vapor pump control

4. Clean-up and Reset

5.1.2 Configuration

This section allows the user to make configurations interactively with the program if needed, and changes front panel indicators as needed. Configurations that require the program to be running while they are input by the user should be implemented here.

Sensor configuration

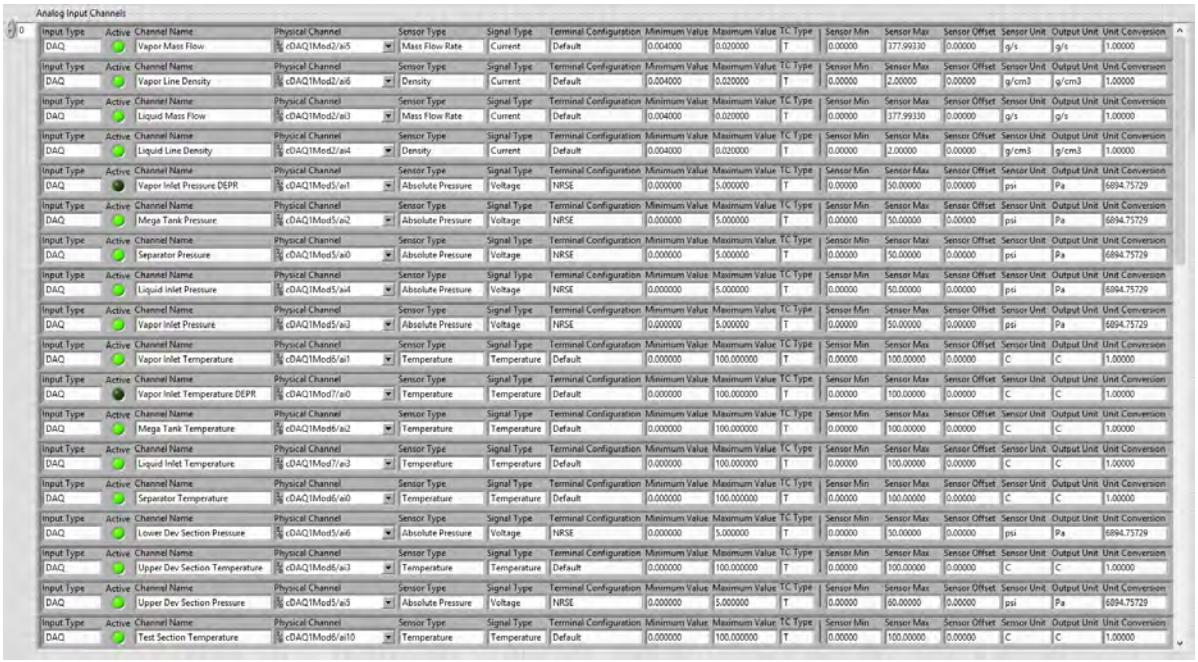

Figure A5.1: List of sensors and their configurations.

Currently, 40 sensors are installed and configured for data acquisition. For convenience and expandability, the sensor configurations are stored as an array of clusters under the *input_channel_task* subVI. Each cluster defines how each sensor is excited and its signal is interpreted. The fields are as follows:

Input Type: only "DAQ" is currently implemented. "Add-on" can be implemented in the future for sensors connected to non-NI systems.

Active: inactive sensors will not be configured.

Channel Name: an alphanumeric identifier. The user should verify this parameter is defined within the printable ASCII set and does not include the *tab* (0x09) character, as it is used later as a CSV file delimiter. No explicit check is performed programmatically.

Physical Channel: the DAQmx physical channel connected to the sensor.

Sensor Type: defines 7 types of sensors: absolute/gauge/differential pressure, temperature, mass flow rate, density, and other. This parameter is not used functionally, but offers ease of identification.

Signal Type: currently supports current (A), voltage (V), and thermocouple (°C) type sensors. The correct DAQmx "Create Channel" VI is used depending on the signal type.

Terminal Configuration: used for voltage measurements only. DAQmx throws an error if an unavailable configuration is selected.

Min/max Value: defines the range of expected analog values. For example, 4-20 mA current sensors would have min/max values of 0.004 and 0.020 A.

TC Type: all DAQmx-supported thermocouple types are available.

Sensor min/max/offset: defines the sensor ratings and offset calibration. This differs from the analog value. For example, a pressure transducer that is rated for 0-50 PSIA but outputs a 4-20 mA current signal has a 0 to 50 psi sensor range, but 4 to 20 analog range.

Sensor/output unit: provides the infrastructure for automatic unit conversion. This functionality is not yet implemented and the conversion factor should be manually specified in the *Unit Conversion* parameter.

Unit Conversion: the conversion multiplied to the sensor output to convert from the sensor unit to the output unit. For example, to convert from mV to V, the unit conversion factor would be 0.001.

Future improvements:

The *input_channel_task* subVI is currently (confusingly) located within the *Measurement Loop* module even though it contains configurations. This is because the configurations are stored directly in a functional subVI. Instead, the configurations should be saved into a file in which the current subVI can read and implement.

Input/Output configurations

Float Switch Physical Channels: defines the polarity and physical channels the pulse generator float switches are connected to. A NI USB-6008 is used for float switch input signals.

Pulse Generator Control Physical Channels: 6 digital output channels are used on another NI USB-6008 to control 6 cartridge heaters in the pulse generator. Another 2 digital output channels are used for driving the stepper motor on the pulse generator. Due to a stepper motor driver—not a controller—that interfaces the motor and LabVIEW, a counter output is required to create the precise pulse train that the driver expects.

Proportional Valve Physical Channels: Three proportional valves (Omega PV series) are controlled using independent 1 to 5 V analog signals. Three NI DAQ analog output channels are used for this function. In the future, these valves can be controlled via the newly installed PLC.

Window Heaters Physical Channels: two programmable power supplies with RS232 serial communication capabilities are used to power the test section window heaters.

PLC Communication: the liquid and vapor positive displacement pumps are controlled by a CLICK PLC via an Ethernet connection.

Trigger thresholds for safety mechanisms

Pulse Generator Heater Safety Values: The cartridge heaters in the pulse generator, with a combined power of 3.8 kW, need to be disabled if the vessel pressure and temperature are too high for a predetermined amount of time. These settings are configured here.

Window Heater Safety Values: A minimum flow rate in the test section is required for the window heaters to be turned on. This is to prevent accidental heating when no flow is present. The minimum flow rate can be changed without stopping the program. Setting a negative value effectively disables this safety feature.

5.1.3 Validation and Initialization

This section is used to validate configurations that were made previously, and initialize important data structures, such as queues, that will be used in the next stage.

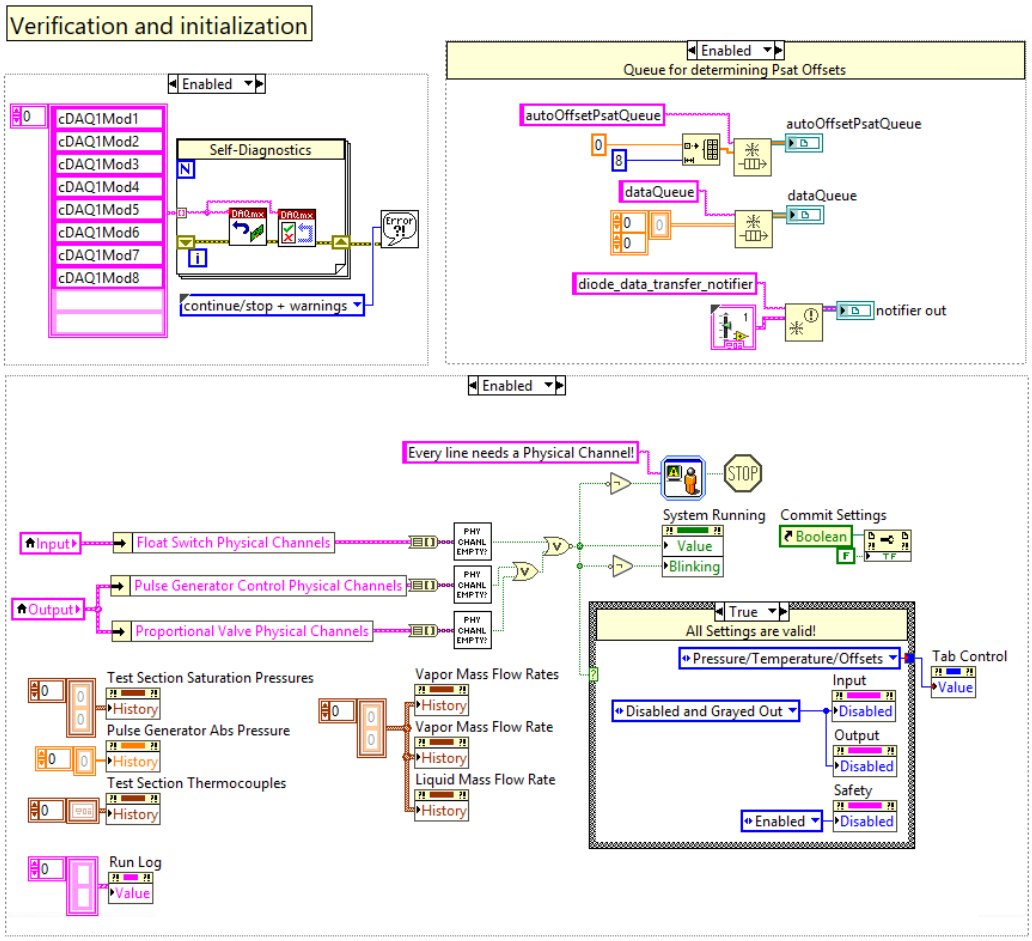

Figure A5.2: Block diagram of the Validation and Initialization section. Configurations are verified and variables are initialized here.

Validate channel configuration—validates the channels configured for each sensor. Currently, the sensor configurations are validated if no channel is configured with a blank physical channel parameter. This can be modified if a different DAQ system or a sensor incompatible with the current DAQ system is implemented.

Initialize front panel control—front panel indicators with sensor data are reinitialized. I/O tabs under the "Settings" page except for the "Safety" tab are grayed out as these settings cannot be modified while the program is running.

Initialize data First-In, First-Out (FIFO) queue—lossless FIFO queues are used to maintain high throughput data sampling. Using queues, the high-speed (2+ kHz) continuous DAQ sample reading loop (i.e main loop) is decoupled from the relatively low-speed data saving process. Since the queue is lossless, its capacity is memory-limited and its performance disk I/O limited.

5.1.4 Measurement Loop

The Measurement Loop is the main loop where measurements are made, equipment is controlled, and data are saved. Safety measures are also implemented in this section. Instead of timing all functions together in a single infinite for-loop, only key functionalities are included in the time-critical main loop. These functionalities include mostly measurement acquisition and processing algorithms. Equipment control and safety mechanisms are decoupled and executed in separate for-loops. This architecture utilizes the multi-threaded execution method built-in to LabVIEW. One key function that is decoupled from the main loop is the data logging system. Since writing a large amount of data to a file tends to be a time consuming operation, a dedicated queue is used to transfer data from a high-speed loop (i.e. the main loop) to a slower one (i.e. data saving loop).

Configure NI-DAQmx driver—sensors connected to the NI-cDAQ chassis are configured using the DAQmx drivers. This is completed in the "input_channel_task.vi". After each sensors is configured, a copy of its configuration parameters and a analog data structure (in the form of a cluster) is generated and included in an array of clusters. This analog data structure includes a CSV-compatible label, offset, raw/converted/average values, and formulas that allow conversion between the raw and converted values.

Prepare front panel indicators—this functionality provides a modular framework to all data-related front panel indicators. In a simple LabVIEW program, values from the DAQmx-Read VI can be wired directly into post-processing algorithms and front panel indicators. Due to the large number of sensors, the complexity of some calculations, and the repeated usage of some sensor data, wiring the signals directly into subVIs and then the front panel indicators will lead to a unmanageable mess[4]. Instead, signal distribution framework is used. Different portions of the front panel indicators are partitioned into sections. The required measured signals for each section are listed by their labels in a cluster with a 1D array. These clusters are then combined into a 1D composite array, which is wired into the "find_label_indices.vi". The array indices of the requested sensor signals as they appear in the order of configured sensors are found and compiled before the start of the continuous collection of the data. This decrease the loop time later on.

Continuously collect sensor data—this is the heart of this program, where data is collected, processed, displayed and queued for logging as needed. The data is first read from the "DAQmx Analog 1D Waveform N-Channel N-Sample" block. The collected waveform includes the raw values for each sensor and is then processed according to the aforementioned conversion formula. Next, the data is enqueued if data logging is activated. Both the raw and converted values, as well as the conversion formulas are saved. Meanwhile, the "data_dist.vi" subVI performs calculations for values that are displayed on the front panel.

[4]This is often known as spaghetti code, which should be avoided.

Test section window heater control—the safety and control sections are separated into two subVIs for ease of management. The test section window heater controller implements two RS232 serial communication lines for the front and back heaters. The heaters are powered by two programmable power supplies, each capable of this communication protocol. A watchdog system that disables the heaters in the case of a program shutdown has yet to implemented. The safety mechanism keeps track of the test section flow rate against safety limits, under which the heaters are disabled.

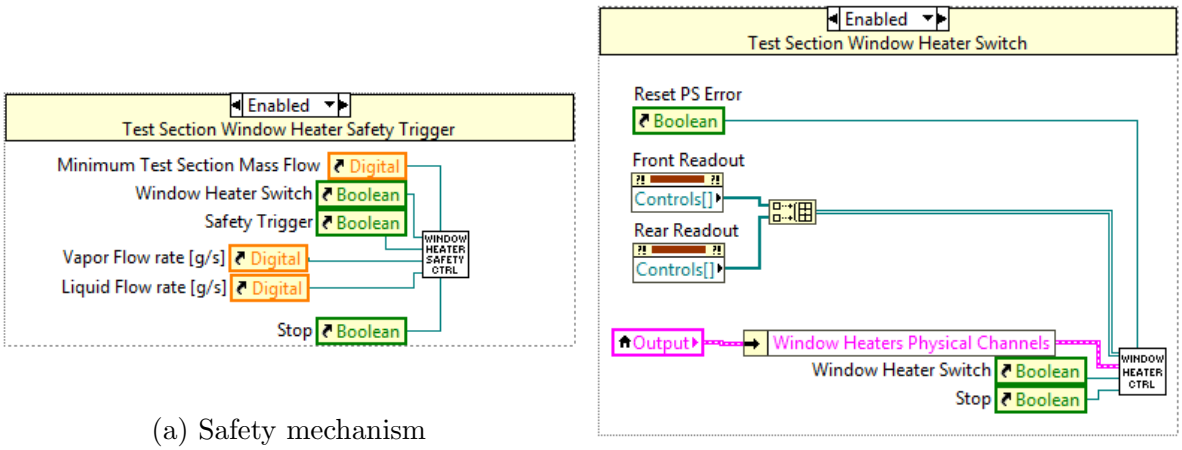

(a) Safety mechanism

(b) Control mechanism

Figure A5.3: Test section heater safety and control mechanisms

Pulse generator control—these are one of the first modules that were implemented during this revision. The control module controls the heaters and the stepper motor, while the safety module monitors the pulse generator pressure and temperature for safe operation.

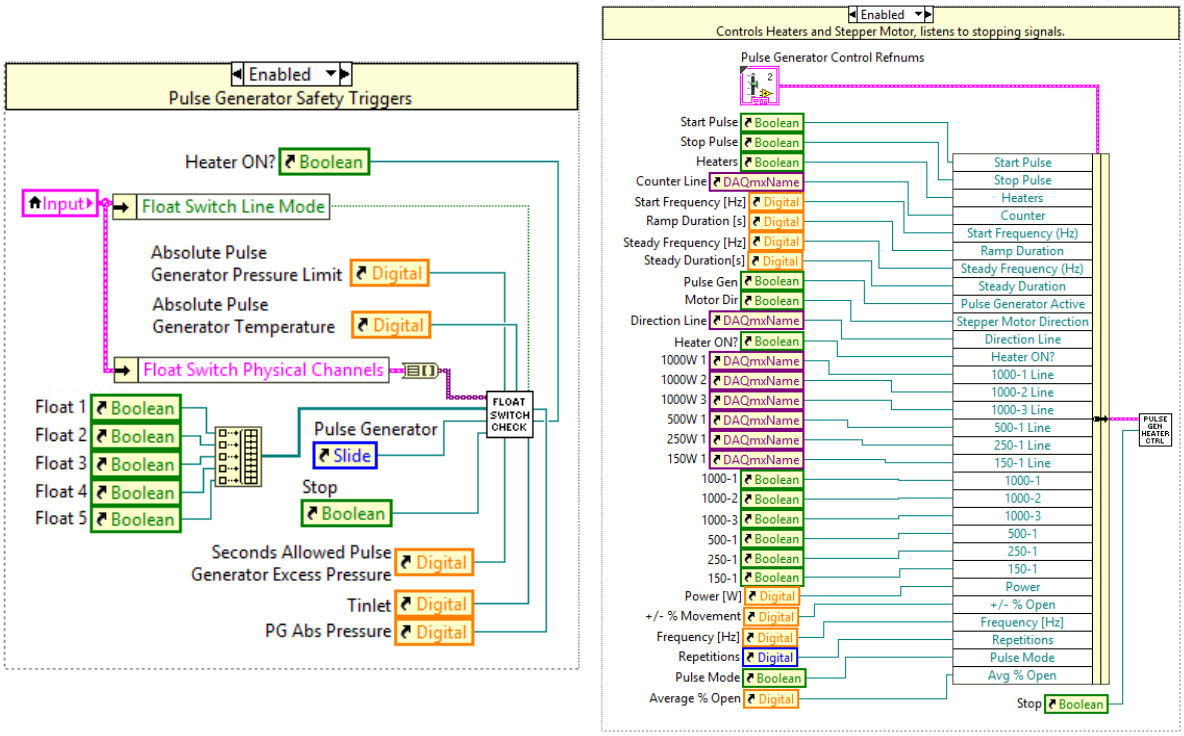

(a) Safety mechanism

(b) Control mechanism

Figure A5.4: Pulse generator heater and stepper motor safety and control mechanisms

Loop data visualization—the concept of a "facility at-a-glance" visualization of the loop operation was brought up during the early stage of the revision process. A proof of concept was implemented where the entire visualization figure is contained in a LabVIEW Typedef and can be updated directly from the block diagram of the main program.

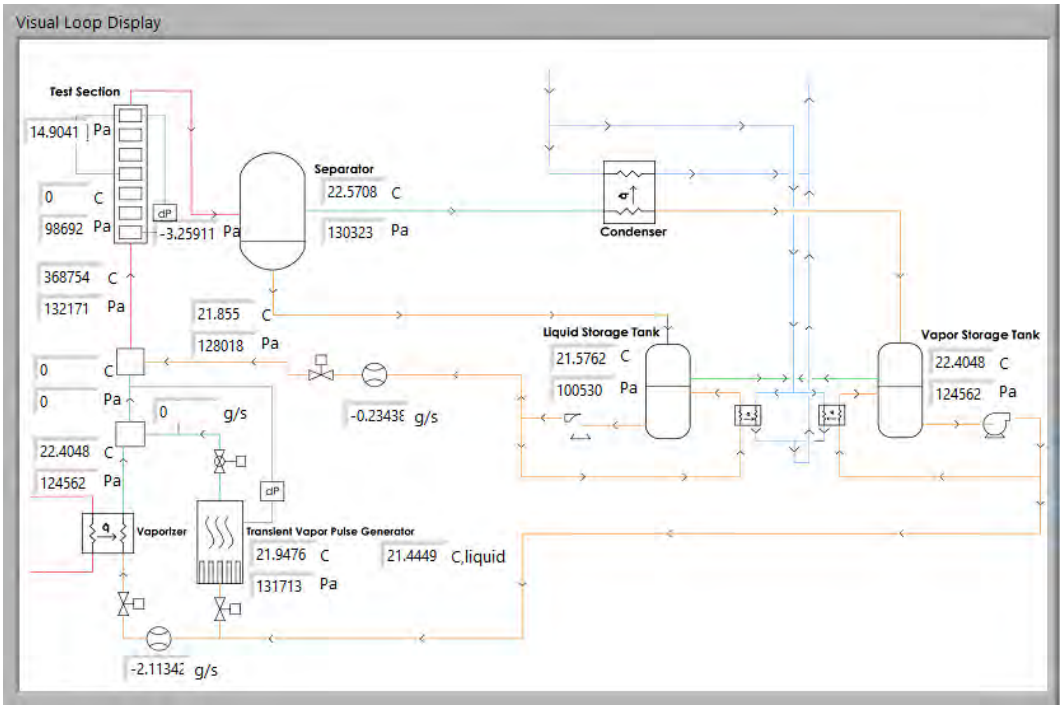

(a) Front Panel

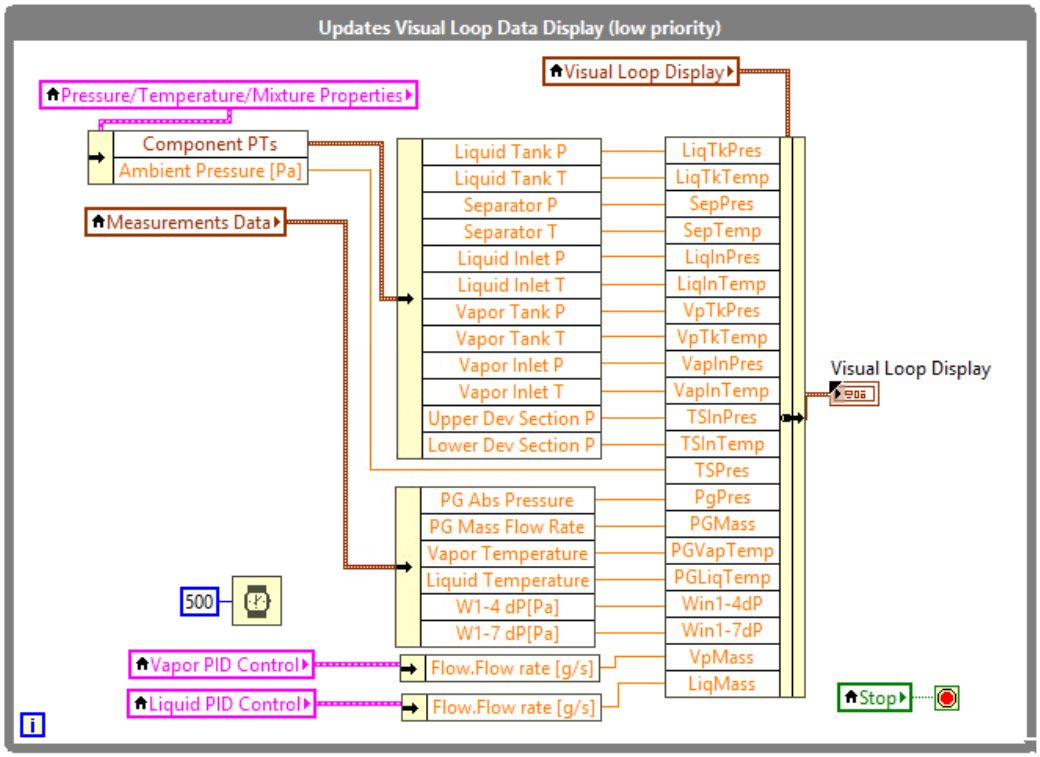

(b) Block Diagram

Figure A5.5: Facility at-a-glance

Loop data logging system—the decoupling of the data logging system from the main loop ensures time-sensitive operations are independent from disk writing operations. This decoupling is implemented via the use of queues. As data is processed in the main loop, it is enqueued if the logging function is activated. In a separate loop, the contents of the queue are constantly monitored and processed in the "write_data.vi" subVI. To further enhance the processing speed, the data is logged to a file in a temporary folder in the operating system before it is copied over to the final destination. This is especially important when the final destination is on the network or the cloud, where repeated open-write-close operations is a bottleneck on execution efficiency.

Sensor offset management—a constant value offset can be applied to each sensor during program execution. Currently, loop conditions are assumed to be saturated before operation. Offsets are applied to non-critical pressure transducers to match the saturation pressures measured by a nearby thermocouple. This can be done with a push of a button labeled "Auto Offset". The automated offsetting algorithm calculates the 30-iteration average of these pressure transducer and thermocouple readings. Currently, 10% of the samples collected per second are processed per iteration. For example, at a sampling frequency of 2000 samples per second (Hz), 200 samples are processed during each loop iteration. This results in a 10 Hz front panel refresh rate. That is, the front panel indicators are updated 10 times a second—a reasonably fast yet legible speed for the operator. The offset values for each parameter can be changed on-the-run from the "offsets" table.

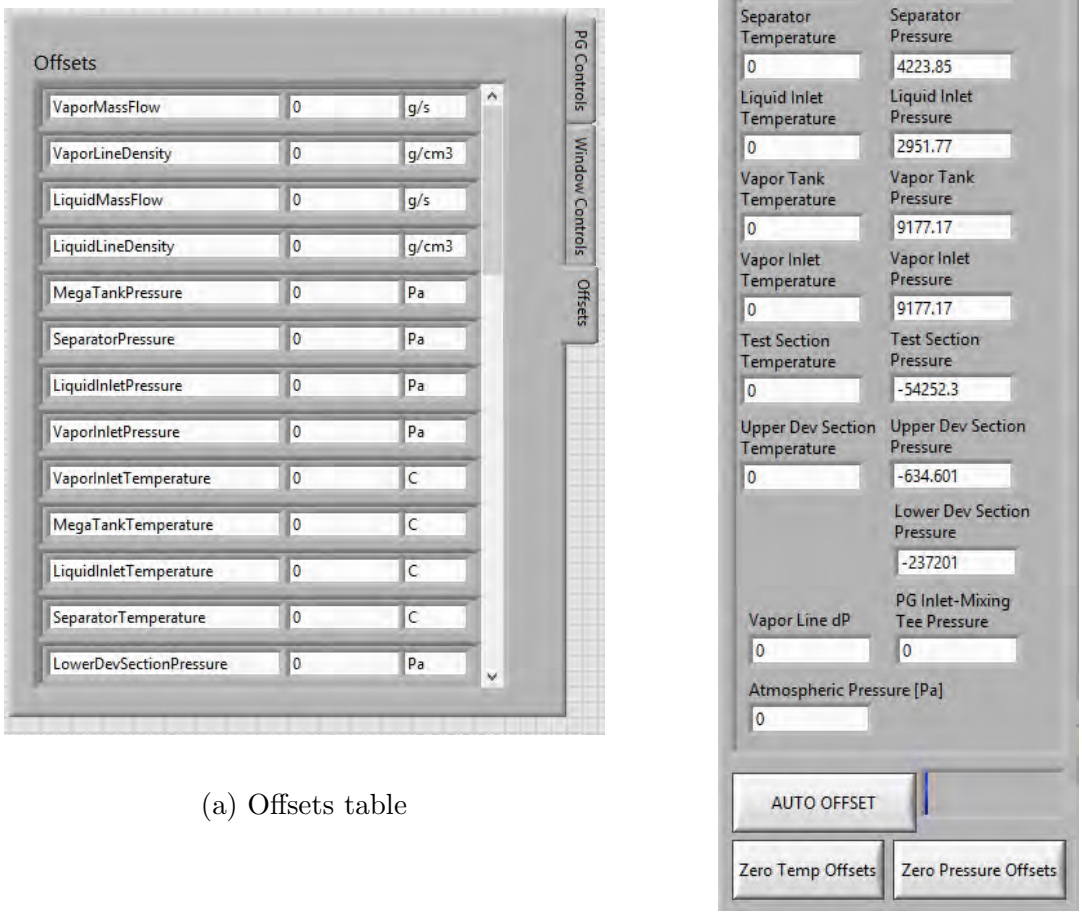

(a) Offsets table

(b) Auto offset system

Figure A5.6: Offset management front panel indicators

Liquid and vapor pump control—the liquid and vapor pumps are used to control the liquid-vapor ratio at the test section inlet. A dedicated for-loop (Figure A5.7) is used to communicate with the PLC via an Ethernet Modbus protocol. Both manual and PID modes are implemented, where the former operates on a percent full capacity basis and the latter on a mass flow rate value. The front panel indicators are shown in Figure A5.8.

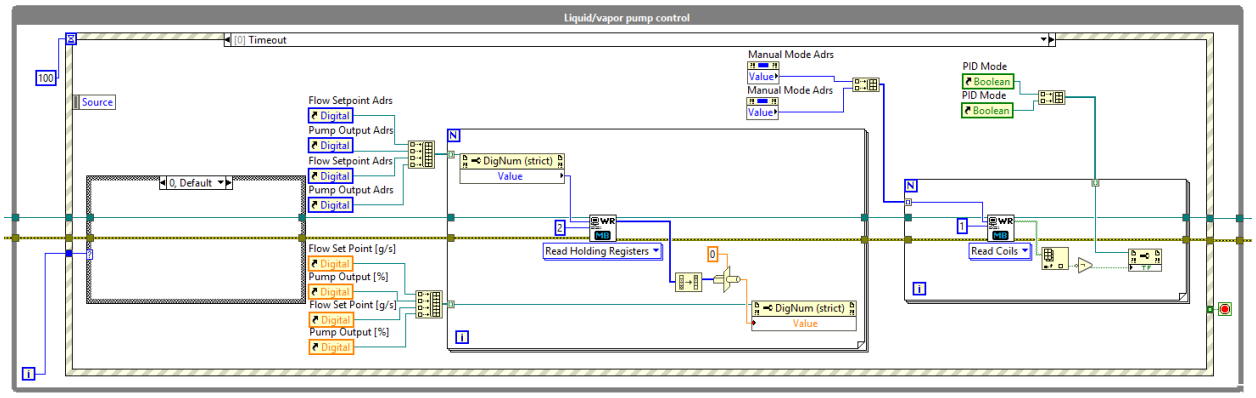

Figure A5.7: Dedicated loop for Modbus communication with the PLC.

Figure A5.8: Front panel controls of the liquid and vapor pumps.

5.1.5 Clean-up and Reset

A complex system such as the annular flow facility involves many moving parts both electrically and mechanically. At the end of an experiment, the system needs to be brought to a known safe state, and front panel controls should be reset for the next time the program is executed. Currently, the task of bringing all system components to a safe state is accomplished in each of the dedicated loops through the use of the "Stop" button reference. While no explicit checks are implemented to pass the Stop button reference, it is passed to all component loops. This way, a single click of the Stop button triggers a dedicated event for each component to be brought to a safe state. By design, only upon completion of all component loops can the Clean-up and Rest module be executed. In this module, front panels are reset. For example, previously grayed-out settings panels are reset and enabled for the next run. While a bare bones design is currently used in this module, more sophisticated checks can be implemented.